# Unified lattice Boltzmann method with improved schemes for multiphase flow simulation: Application to droplet dynamics under realistic conditions

Geng Wang,[1] Linlin Fei,[2,*] and Kai H. Luo[1,†]

[1]*Department of Mechanical Engineering, University College London, Torrington Place, London WC1E 7JE, United Kingdom*

[2]*Chair of Building Physics, Department of Mechanical and Process Engineering, ETH Zürich (Swiss Federal Institute of Technology in Zürich), Zürich 8092, Switzerland*

(Received 30 November 2021; accepted 25 March 2022; published 20 April 2022)

As a powerful mesoscale approach, the lattice Boltzmann method (LBM) has been widely used for the numerical study of complex multiphase flows. Recently, Luo *et al.* [Philos. Trans. R. Soc. A: Math. Phys. Eng. Sci. **379**, 20200397 (2021)] proposed a unified lattice Boltzmann method (ULBM) to integrate the widely used lattice Boltzmann collision operators into a unified framework. In this study, we incorporate additional features into this ULBM in order to simulate multiphase flow under realistic conditions. A nonorthogonal moment set [Fei *et al.*, Phys. Rev. E **97**, 053309 (2018)] and the entropic-multi-relaxation-time (KBC) lattice Boltzmann model are used to construct the collision operator. An extended combined pseudopotential model is proposed to realize multiphase flow simulation at high-density ratio with tunable surface tension over a wide range. The numerical results indicate that the improved ULBM can significantly decrease the spurious velocities and adjust the surface tension without appreciably changing the density ratio. The ULBM is validated through reproducing various droplet dynamics experiments, such as binary droplet collision and droplet impingement on superhydrophobic surfaces. Finally, the extended ULBM is applied to complex droplet dynamics, including droplet pancake bouncing and droplet splashing. The maximum Weber number and Reynolds number in the simulation reach 800 and 7200, respectively, at a density ratio of 1000. The study demonstrates the generality and versatility of ULBM for incorporating schemes to tackle challenging multiphase problems.

DOI: 10.1103/PhysRevE.105.045314

## I. INTRODUCTION

The breakup, merging, and deformation of the liquid droplet are ubiquitous multiphase phenomena in engineering, material science, and medical science [1]. Gaining a thorough understanding of droplet dynamics could benefit a wide range of applications, such as the anti-icing of the turbine blade [2,3], inkjet printing [4,5], and spray cooling [6]. However, the multiphase interface dynamics is a typical nonlinear, nonequilibrium, and multiscale phenomenon, which is further complicated by coupling with heat transfer and phase-change process. For such a process, it is often challenging for experimental techniques to quantify the key dynamic parameters, hampering the detailed analysis of mechanisms behind. Thus, advanced numerical research methods are needed to complement the analysis [7].

Conventional numerical methods for multiphase flows are based on numerical solutions of the continuum-based macroscopic governing equations, supplemented by interface capturing schemes such as the volume of fluid and the level-set method. In contrast, the lattice Boltzmann method (LBM) solves a set of discrete Boltzmann equations for distribution functions, which recovers the Navier-Stokes (N-S) equations in the macroscopic limit [8,9]. The LBM is advantageous for the study of multiphase flows, mainly because its kinetic nature allows natural incorporation of microscale and mesoscale physics such as the phase interface breakup, merging, and deformation [9–11]. Consequently, the LBM has achieved remarkable success in simulating various complex multiphase (multicomponent) flows and phase-change phenomena [9,12–14].

Numerous multiphase LB models have been proposed in the past three decades [15–18], among which the pseudopotential LBM has become one of the most popular models mainly owing to its conceptual simplicity and computational efficiency [7,11]. The key component of the pseudopotential model is the forcing term describing the interaction force between different phases. However, the classical pseudopotential model [18], implemented with a single-relaxation time (SRT) collision operator and the "velocity-shift" forcing model, has several drawbacks, such as high spurious velocities [19], thermodynamic inconsistency [20], and surface tension dependence on the density ratio [21].

In the past decade, considerable efforts have been made to overcome the above-mentioned drawbacks. The advances made can be generally divided into two families: (i) Improved collision operators, such as central-moment-based algorithm (CLBM) [22,23], multiple-relaxation time (MRT) LBM [24,25], and the entropic lattice Boltzmann (ELB) method [26,27]; (ii) Improved forcing models, like the multirange pseudopotential model by Sbragaglia *et al.* [19], and the exact-difference method to incorporate the forcing field by

*Corresponding author: linfei@ethz.ch

†Corresponding author: k.luo@ucl.ac.uk

 

Kupershtokh *et al.* [28]. In addition, Li *et al.* [21,24] proposed additional forcing terms to tune surface tension and restore the thermodynamic consistency. Furthermore, a high-order forcing scheme was proposed by Lycett-Brown and Luo [29] for the simulation of multiphase flow with large density ratio and tunable surface tension. With optimized choices of collision operators and forcing models, the pseudopotential LBM has been successfully applied to investigate droplet dynamics under a variety of conditions [12,30]. In practice, however, making a choice and switching between models are not easy, without a unified modeling framework. To this aim, Luo *et al.* [31] proposed a unified lattice Boltzmann model (ULBM), which integrates the widely used collision operators into a unified framework, with the most popular forcing models implemented. The ULBM allows the straightforward switch between different collision operators and/or forcing schemes. Developed LB models can also be easily incorporated into the general framework of ULBM.

To study droplet dynamics over a wide range of physical parameters, in this study, the nonorthogonal moment set [32] and KBC-ELB model [27] are combined to construct a collision operator. Besides, based on the recent development by Kharmiani *et al.* [33], we propose an extended combined pseudopotential (ECP) multiphase model to achieve large density ratio as well as independent surface tension adjustment. These developments are seamlessly integrated into the ULBM framework. Finally, we test the capability of the extended ULBM in modeling the complex droplet dynamics, such as droplet pancake bouncing and droplet collision splashing, against experimental and other numerical results. The rest of the paper is structured as follows: Sec. II provides details of the ULBM and model developments. Section III presents the assessment of the proposed models and conducts comprehensive model validations against various experimental results. It is demonstrated that the present enriched ULBM is capable of simulating droplet dynamics over a wide range of realistic physical parameters with complex boundary conditions. The conclusions of this study are given in Sec. IV.

## II. METHODOLOGY

### A. ULBM with KBC-ELB collision operator

The LB evolution equation in the ULBM framework with forcing term can be written as

$$\begin{aligned} f_i(\boldsymbol{x}+\boldsymbol{e}_i\Delta t, t+\Delta t) &\equiv f_i^*(\boldsymbol{x},t) \\ &= \mathbf{M}^{-1}\mathbf{N}^{-1}(\mathbf{I}-\mathbf{S})\mathbf{N}\mathbf{M}f_i(\boldsymbol{x},t) + \mathbf{M}^{-1}\mathbf{N}^{-1}\mathbf{S}\mathbf{N}\mathbf{M}f_i^{\mathrm{eq}}(\boldsymbol{x},t) \\ &+ \mathbf{M}^{-1}\mathbf{N}^{-1}(\mathbf{I}-\mathbf{S}/2)\mathbf{N}\mathbf{M}\Delta t|R_i\rangle, \end{aligned} \tag{1}$$

where $f_i$ and $f_i^*$ indicate the precollision and postcollision discrete distribution functions, respectively. $f_i^{\mathrm{eq}}$ is the equilibrium distribution function and $|R_i\rangle$ is the discrete forcing term. $\boldsymbol{e}_i$ and $\Delta t = 1$ are the discrete velocity and the time step, respectively. In this study, we focus on three-dimensional (3D) simulations and the D3Q27 discrete velocity model ($\boldsymbol{e_i} = [|e_{ix}\rangle, |e_{iy}\rangle, |e_{iz}\rangle]$) is used [34]:

$$\begin{aligned} |e_{ix}\rangle &= [0,1,-1,0,0,0,0,1,-1,1,-1,1,-1,1, \\ &\quad -1,0,0,0,0,1,-1,1,-1,1,-1,1,-1]^{\mathrm{T}}, \\ |e_{iy}\rangle &= [0,0,0,1,-1,0,0,1,1,-1,-1,0,0,0,0,1, \\ &\quad -1,1,-1,1,1,-1,-1,1,1,-1,-1]^{\mathrm{T}}, \\ |e_{iz}\rangle &= [0,0,0,0,0,1,-1,0,0,0,0,1,1,-1,-1,1,1, \\ &\quad -1,-1,1,1,1,1,-1,-1,-1,-1]^{\mathrm{T}}, \end{aligned}$$

where $i = 0 \ldots 27$ and $|\cdot\rangle$ donates a 27-column vector, and the superscript T is the transposition symbol. In Eq. (1), **I** is the unit matrix, and **S** represents the relaxation matrix that contains the relaxation parameters for various moments. In addition, the transformation matrix **M** is adopted to transform the distribution functions ($f_i$) to their raw moments ($T_i$). The shift matrix **N** is used to shift the raw moments into the central moments ($\tilde{T}_i$), and the transformation/shift can be expressed as

$$|f_i\rangle = \mathbf{M}^{-1}|T_i\rangle = \mathbf{M}^{-1}\mathbf{N}^{-1}|\tilde{T}_i\rangle. \tag{2}$$

In this study, we adopt the nonorthogonal moments proposed by Fei *et al.* [32,35] to construct the collision operator. Compared with the traditional orthogonal moments, the nonorthogonal moments lead to computational cost reduction while retaining the algorithm robustness [12,36]. We first define the raw moment as

$$k_{pqn} = \sum f_i e_{ix}^p e_{iy}^q e_{iz}^n, \;\; p,q,n \in \{0,1,2\}, \tag{3}$$

and the central moment as

$$\begin{aligned} \tilde{k}_{pqn} &= \sum f_i (e_{ix}-u_x)^p (e_{iy}-u_y)^q (e_{iz}-u_z)^n, \\ &\quad p,q,n \in \{0,1,2\}, \end{aligned} \tag{4}$$

where $u_x$, $u_y$, and $u_z$ are the velocity components in $x$, $y$, and $z$ directions, respectively. The nonorthogonal raw moment set can be written as follows, where the subscript of moments is in ascending order of $(p+q+n)$:

$$\begin{aligned} |T_i\rangle = \mathbf{M}f_i[&k_{000},\, k_{100},\, k_{010},\, k_{001},\, k_{110},\, k_{101},\, k_{011},\, k_{200} \\ &+ k_{020} + k_{002},\, k_{200} - k_{020},\, k_{200} - k_{002},\, k_{120}, \\ &k_{102}, k_{210}, k_{201}, k_{012}, k_{021}, k_{111}, k_{220}, k_{202}, k_{022}, k_{211}, \\ &k_{121}, k_{112}, k_{122}, k_{212}, k_{221}\, , k_{222}]^{\mathrm{T}}, \end{aligned} \tag{5}$$

The corresponding central moment set is

$$\begin{aligned} |\tilde{T}_i\rangle = \mathbf{N}\mathbf{M}f_i = [&\tilde{k}_{000},\, \tilde{k}_{100},\, \tilde{k}_{010},\, \tilde{k}_{001},\, \tilde{k}_{110},\, \tilde{k}_{101},\, \tilde{k}_{011},\, \tilde{k}_{200} \\ &+ \tilde{k}_{020} + \tilde{k}_{002},\, \tilde{k}_{200} - \tilde{k}_{020},\, \tilde{k}_{200} - \tilde{k}_{002},\, \tilde{k}_{120},\, \tilde{k}_{102}, \\ &\tilde{k}_{210},\, \tilde{k}_{201},\, \tilde{k}_{012},\, \tilde{k}_{021},\, \tilde{k}_{111},\, \tilde{k}_{220},\, \tilde{k}_{202},\, \tilde{k}_{022},\, \tilde{k}_{211}, \\ &\tilde{k}_{121},\, \tilde{k}_{112},\, \tilde{k}_{122},\, \tilde{k}_{212},\, \tilde{k}_{221},\, \tilde{k}_{222}]^{\mathrm{T}}. \end{aligned} \tag{6}$$

Different from the original nonorthogonal moment set in Ref. [32], we keep the trace of the stress tensor $(k_{200}+k_{020}+k_{002})$ and the normal stress differences at unit density $(k_{200}-k_{020}, k_{200}-k_{002})$ for the ease of incorporation of KBC collision operator. The corresponding

transformation matrix **M** can be obtained by Eqs. (3) and (5):

$$\mathbf{M} = \begin{bmatrix}
1 & 1 & 1 & 1 & 1 & 1 & 1 & 1 & 1 & 1 & 1 & 1 & 1 & 1 & 1 & 1 & 1 & 1 & 1 & 1 & 1 & 1 & 1 & 1 & 1 & 1 & 1 \\
0 & 1 & -1 & 0 & 0 & 0 & 0 & 1 & -1 & 1 & -1 & 1 & -1 & 1 & -1 & 0 & 0 & 0 & 0 & 1 & -1 & 1 & -1 & 1 & -1 & 1 & -1 \\
0 & 0 & 0 & 1 & -1 & 0 & 0 & 1 & 1 & -1 & -1 & 0 & 0 & 0 & 0 & 1 & -1 & 1 & -1 & 1 & 1 & -1 & -1 & 1 & 1 & -1 & -1 \\
0 & 0 & 0 & 0 & 0 & 1 & -1 & 0 & 0 & 0 & 0 & 1 & 1 & -1 & -1 & 1 & 1 & -1 & -1 & 1 & 1 & 1 & 1 & -1 & -1 & -1 & -1 \\
0 & 0 & 0 & 0 & 0 & 0 & 0 & 1 & -1 & -1 & 1 & 0 & 0 & 0 & 0 & 0 & 0 & 0 & 0 & 1 & -1 & -1 & 1 & 1 & -1 & -1 & 1 \\
0 & 0 & 0 & 0 & 0 & 0 & 0 & 0 & 0 & 0 & 0 & 1 & -1 & -1 & 1 & 0 & 0 & 0 & 0 & 1 & -1 & 1 & -1 & -1 & 1 & -1 & 1 \\
0 & 0 & 0 & 0 & 0 & 0 & 0 & 0 & 0 & 0 & 0 & 0 & 0 & 0 & 0 & 1 & -1 & -1 & 1 & 1 & 1 & -1 & -1 & -1 & -1 & 1 & 1 \\
0 & 1 & 1 & 1 & 1 & 1 & 1 & 2 & 2 & 2 & 2 & 2 & 2 & 2 & 2 & 2 & 2 & 2 & 2 & 3 & 3 & 3 & 3 & 3 & 3 & 3 & 3 \\
0 & 1 & 1 & -1 & -1 & 0 & 0 & 0 & 0 & 0 & 0 & 1 & 1 & 1 & 1 & -1 & -1 & -1 & -1 & 0 & 0 & 0 & 0 & 0 & 0 & 0 & 0 \\
0 & 1 & 1 & 0 & 0 & -1 & -1 & 1 & 1 & 1 & 1 & 0 & 0 & 0 & 0 & -1 & -1 & -1 & -1 & 0 & 0 & 0 & 0 & 0 & 0 & 0 & 0 \\
0 & 0 & 0 & 0 & 0 & 0 & 0 & 1 & -1 & 1 & -1 & 0 & 0 & 0 & 0 & 0 & 0 & 0 & 0 & 1 & -1 & 1 & -1 & 1 & -1 & 1 & -1 \\
0 & 0 & 0 & 0 & 0 & 0 & 0 & 0 & 0 & 0 & 0 & 1 & -1 & 1 & -1 & 0 & 0 & 0 & 0 & 1 & -1 & 1 & -1 & 1 & -1 & 1 & -1 \\
0 & 0 & 0 & 0 & 0 & 0 & 0 & 1 & 1 & -1 & -1 & 0 & 0 & 0 & 0 & 0 & 0 & 0 & 0 & 1 & 1 & -1 & -1 & 1 & 1 & -1 & -1 \\
0 & 0 & 0 & 0 & 0 & 0 & 0 & 0 & 0 & 0 & 0 & 1 & 1 & -1 & -1 & 0 & 0 & 0 & 0 & 1 & 1 & 1 & 1 & -1 & -1 & -1 & -1 \\
0 & 0 & 0 & 0 & 0 & 0 & 0 & 0 & 0 & 0 & 0 & 0 & 0 & 0 & 0 & 1 & -1 & 1 & -1 & 1 & 1 & -1 & -1 & 1 & 1 & -1 & -1 \\
0 & 0 & 0 & 0 & 0 & 0 & 0 & 0 & 0 & 0 & 0 & 0 & 0 & 0 & 0 & 1 & 1 & -1 & -1 & 1 & 1 & 1 & 1 & -1 & -1 & -1 & -1 \\
0 & 0 & 0 & 0 & 0 & 0 & 0 & 0 & 0 & 0 & 0 & 0 & 0 & 0 & 0 & 0 & 0 & 0 & 0 & 1 & -1 & -1 & 1 & -1 & 1 & 1 & -1 \\
0 & 0 & 0 & 0 & 0 & 0 & 0 & 1 & 1 & 1 & 1 & 0 & 0 & 0 & 0 & 0 & 0 & 0 & 0 & 1 & 1 & 1 & 1 & 1 & 1 & 1 & 1 \\
0 & 0 & 0 & 0 & 0 & 0 & 0 & 0 & 0 & 0 & 0 & 1 & 1 & 1 & 1 & 0 & 0 & 0 & 0 & 1 & 1 & 1 & 1 & 1 & 1 & 1 & 1 \\
0 & 0 & 0 & 0 & 0 & 0 & 0 & 0 & 0 & 0 & 0 & 0 & 0 & 0 & 0 & 1 & 1 & 1 & 1 & 1 & 1 & 1 & 1 & 1 & 1 & 1 & 1 \\
0 & 0 & 0 & 0 & 0 & 0 & 0 & 0 & 0 & 0 & 0 & 0 & 0 & 0 & 0 & 0 & 0 & 0 & 0 & 1 & 1 & -1 & -1 & -1 & -1 & 1 & 1 \\
0 & 0 & 0 & 0 & 0 & 0 & 0 & 0 & 0 & 0 & 0 & 0 & 0 & 0 & 0 & 0 & 0 & 0 & 0 & 1 & -1 & 1 & -1 & -1 & 1 & -1 & 1 \\
0 & 0 & 0 & 0 & 0 & 0 & 0 & 0 & 0 & 0 & 0 & 0 & 0 & 0 & 0 & 0 & 0 & 0 & 0 & 1 & -1 & -1 & 1 & 1 & -1 & -1 & 1 \\
0 & 0 & 0 & 0 & 0 & 0 & 0 & 0 & 0 & 0 & 0 & 0 & 0 & 0 & 0 & 0 & 0 & 0 & 0 & 1 & -1 & -1 & 1 & -1 & 1 & 1 & -1 \\
0 & 0 & 0 & 0 & 0 & 0 & 0 & 0 & 0 & 0 & 0 & 0 & 0 & 0 & 0 & 0 & 0 & 0 & 0 & 1 & 1 & 1 & -1 & -1 & -1 & -1 & -1 \\
0 & 0 & 0 & 0 & 0 & 0 & 0 & 0 & 0 & 0 & 0 & 0 & 0 & 0 & 0 & 0 & 0 & 0 & 0 & 1 & 1 & 1 & 1 & 1 & 1 & 1 & 1
\end{bmatrix}.$$

The shift matrix **N** for this nonorthogonal moment set is calculated by the same approach in Ref. [32]. The explicit expressions of **M**, **N**, $\mathbf{M}^{-1}$, $\mathbf{N}^{-1}$ for the D3Q19 and D3Q27 nonorthogonal moment set can be found in the Supplemental Material [37].

Following the choices in CLBM [23,32,38,39], the discrete equilibrium central moments are set equal to the integral central moments of the continuous Maxwell-Boltzmann distribution, i.e.,

$$\begin{aligned}\tilde{k}^{\mathrm{eq}}_{pqn} &= \sum f_i^{\mathrm{eq}}(e_{ix}-u_x)^p(e_{iy}-u_y)^q(e_{iz}-u_z)^n \\ &= \int_{-\infty}^{+\infty}\int_{-\infty}^{+\infty}\int_{-\infty}^{+\infty} f_M(\zeta_x-u_x)^p(\zeta_y-u_y)^q(\zeta_z-u_z)^n d\zeta_x d\zeta_y d\zeta_z,\end{aligned} \tag{7}$$

where $f_M$ is the Maxwell-Boltzmann distribution in the continuous velocity space $\zeta = [\zeta_x, \zeta_y, \zeta_z]$:

$$f_M(\rho, \boldsymbol{u}, \zeta) = \frac{\rho}{2\pi C_S^2}\exp\left[-\frac{(\zeta-\boldsymbol{u})^2}{2C_S^2}\right], \tag{8}$$

Substituting Eqs. (7) and (8) into the definition in Eq. (6), we can obtain:

$$\left|\tilde{\mathrm{T}}_i^{\mathrm{eq}}\right\rangle = \mathbf{N}\mathbf{M}f_i^{\mathrm{eq}} = \left[\rho, 0, 0, 0, 0, 0, 0, 3\rho C_S^2, 0, 0, 0, 0, 0, 0, 0, 0, 0, \rho C_S^4, \rho C_S^4, \rho C_S^4, 0, 0, 0, 0, 0, 0, \ \rho C_S^6\right]^{\mathrm{T}}. \tag{9}$$

Consistently, the discrete forcing terms in the central moment space are defined as the integral of the forcing effect in the Boltzmann equation [32,39]:

$$C_i = \sum R_i(e_{ix}-u_x)^p(e_{iy}-u_y)^q(e_{iz}-u_z)^n = \int_{-\infty}^{+\infty}\int_{-\infty}^{+\infty}\int_{-\infty}^{+\infty} R_M(\zeta_x-u_x)^p(\zeta_y-u_y)^q(\zeta_z-u_z)^n d\zeta_x d\zeta_y d\zeta_z, \tag{10}$$

where the forcing effect in the Boltzmann equation is given approximatively by He *et al.* [40]:

$$R_M = \frac{(\zeta-\boldsymbol{u})\cdot\boldsymbol{F}}{\rho C_S^2} f_M. \tag{11}$$

Substituting Eqs. (10) and (11), the forcing terms in central moment space ($|C_i\rangle$) can be written as:

$$\begin{aligned}|C_i\rangle &= \mathbf{N}\mathbf{M}|R_i\rangle \\ &= \big[0, F_x, F_y, F_z, 0, 0, 0, 0, 0, 0, F_xC_S^2, F_xC_S^2, F_yC_S^2, \\ &\quad F_zC_S^2, F_yC_S^2, F_zC_S^2, 0, 0, 0, 0, 0, 0, 0, F_xC_S^4, \\ &\quad F_yC_S^4, F_yC_S^4, 0\big]^{\mathrm{T}}.\end{aligned} \tag{12}$$

where $\mathbf{F} = [F_x, F_y, F_z]$ represents the forcing field, and $C_S = \sqrt{1/3}$ is the lattice sound speed. In the recent work of Fei *et al.* [35], they used the same nonorthogonal moment set in an MRT framework, which is equivalent to a ULBM version [Eq. (1)] with a unit shift matrix **N**. And, the relaxation matrix in their work is set as

$$\begin{aligned}\mathbf{S} = \mathrm{diag}(0, 1, 1, 1, s_v, s_v, s_v, s_b, s_v, s_v, s_3, s_3, s_3, s_3, s_3, s_3, \\ s_{3b}, s_4, s_4, s_4, s_{4b}, s_{4b}, s_{4b}, s_5, s_5, s_5, s_6).\end{aligned} \tag{13}$$

where $s_v$ and $s_b$ are the relaxation parameters for the second-order moments, whose values depend on the fluid kinematic and bulk viscosities [$\nu = (1/s_v - 0.5)C_S^2\Delta t$, $\xi = 2/3(1/s_b - 0.5)C_S^2\Delta t$, where $\nu$ and $\xi$ are the fluid kine-

TABLE I. The relaxation matrix for various collision operators in the ULBM framework.

| Collison operators | Relaxation matrix (S) |
|---|---|
| SRT [31] | $\mathbf{S} = \mathrm{diag}(0, 1, 1, 1, s_v, s_v, s_v, s_v, s_v, s_v, s_v, s_v, s_v, s_v, s_v, s_v, s_v, s_v, s_v, s_v, s_v, s_v, s_v, s_v, s_v, s_v, s_v).$ |
| KBC [41] | $\mathbf{S} = \mathrm{diag}(0, 1, 1, 1, s_v, s_v, s_v, s_v\gamma, s_v, s_v, s_v\gamma, s_v\gamma, s_v\gamma, s_v\gamma, s_v\gamma, s_v\gamma, s_v\gamma, s_v\gamma, s_v\gamma, s_v\gamma, s_v\gamma, s_v\gamma, s_v\gamma, s_v\gamma, s_v\gamma, s_v\gamma, s_v\gamma).$ |
| Standard regularized LB(RLB) [48] | $\mathbf{S} = \mathrm{diag}(0, 1, 1, 1, s_v, s_v, s_v, s_v, s_v, s_v, 1, 1, 1, 1, 1, 1, 1, 1, 1, 1, 1, 1, 1, 1, 1, 1, 1).$ |
| CLBM [32] | $\mathbf{S} = \mathrm{diag}(0, 1, 1, 1, s_v, s_v, s_v, s_b, s_v, s_v, s_3, s_3, s_3, s_3, s_3, s_3, s_{3b}, s_4, s_4, s_4, s_{4b}, s_{4b}, s_{4b}, s_5, s_5, s_5, s_6).$ |
| ELBM [66] | $\mathbf{S} = \mathrm{diag}(0, 1, 1, 1, s_v\gamma, s_v\gamma, s_v\gamma, s_v\gamma, s_v\gamma, s_v\gamma, s_v\gamma, s_v\gamma, s_v\gamma, s_v\gamma, s_v\gamma, s_v\gamma, s_v\gamma, s_v\gamma, s_v\gamma, s_v\gamma, s_v\gamma, s_v\gamma, s_v\gamma, s_v\gamma, s_v\gamma, s_v\gamma, s_v\gamma).$ |

matic and bulk viscosities, respectively]. The other relaxation parameters for higher-order moments can be chosen freely.

In this paper, we further incorporate the KBC model into ULBM which is originally proposed in Ref. [27]. The key idea of the KBC model is to relax the high-order moments (including $k_{200} + k_{020} + k_{002}$ and all the moments with $p + q + n \geqslant 3$ in Eq. (6) in the present work) recurring to an entropic stabilizer given by the maximum entropy condition. More specifically, the relaxation parameters which correspond to the high-order moments in Eq. (13) need to be modified as $s_v\gamma$. And, the entropic stabilizer $\gamma$ based on the entropic stabilizing condition, is obtained by [27,41]

$$\gamma = \frac{1}{s_v} - \left(1 - \frac{1}{s_v}\right) \sum_i \frac{\Delta s_i \Delta h_i}{f_i^{\mathrm{eq}}} \Bigg/ \sum_i \frac{\Delta h_i \Delta h_i}{f_i^{\mathrm{eq}}}, \tag{14}$$

where $s_i$ and $h_i$ are the shear part and high-order part of the distribution function, respectively. $\Delta s_i = s_i - s_i^{\mathrm{eq}}$ and $\Delta h_i = h_i - h_i^{\mathrm{eq}}$ are the deviations, and the superscript *eq* denotes the equilibrium state. Usually, the shear part includes the second-order moments. In this study, the shear-part moments are chosen as the off-diagonal components $(\tilde{k}_{110}, \tilde{k}_{101}, \tilde{k}_{011})$ and the normal stress differences $(\tilde{k}_{200} - \tilde{k}_{020}, \tilde{k}_{200} - \tilde{k}_{200})$ in central moments, which can be written as

$$\begin{aligned} |\tilde{\mathrm{T}}_{si}\rangle = {} & [0, 0, 0, 0, \tilde{k}_{110}, \tilde{k}_{101}, \tilde{k}_{011}, 0, \tilde{k}_{200} \\ & - \tilde{k}_{020}, \tilde{k}_{200} - \tilde{k}_{200}, 0,\ 0,\ 0,\ 0,\ 0,\ 0,\ 0,\ 0,\ 0,\ 0,\ 0, \\ & 0,\ 0,\ 0,\ 0,\ 0,\ 0]^{\mathrm{T}}, \end{aligned} \tag{15}$$

and the corresponding high-order part moments are

$$\begin{aligned} |\tilde{\mathrm{T}}_{hi}\rangle = {} & [0,\ 0,\ 0,\ 0,\ 0,\ 0,\ 0,\ \tilde{k}_{200} + \tilde{k}_{020} \\ & + \tilde{k}_{002},\ 0,\ 0,\ \tilde{k}_{120},\ \tilde{k}_{102},\ \tilde{k}_{210},\ \tilde{k}_{210},\ \tilde{k}_{012},\ \tilde{k}_{021},\ \tilde{k}_{111}, \\ & \tilde{k}_{220},\ \tilde{k}_{202},\ \tilde{k}_{022},\ \tilde{k}_{211},\ \tilde{k}_{121},\ \tilde{k}_{112},\ \tilde{k}_{122},\ \tilde{k}_{212},\ \tilde{k}_{221}, \\ & \tilde{k}_{222}]^{\mathrm{T}}. \end{aligned} \tag{16}$$

For the KBC model, the relaxation parameters are modified as

$$\begin{aligned} \mathbf{S} = {} & \mathrm{diag}(0, 1, 1, 1, s_v, s_v, s_v, s_v\gamma, s_v, s_v, s_v\gamma, s_v\gamma, s_v\gamma, s_v\gamma, \\ & s_v\gamma, s_v\gamma, s_v\gamma, s_v\gamma, s_v\gamma, s_v\gamma, s_v\gamma, s_v\gamma, s_v\gamma, s_v\gamma, s_v\gamma, \\ & s_v\gamma, s_v\gamma). \end{aligned} \tag{17}$$

It is noted that for the current model, the relaxation parameters are all determined by the liquid viscosities and the maximum entropy theory. One significant advance of the present ULBM is that the optimized relaxation parameters are self-adaptive at each lattice node at every time step rather than being obtained by the trial and error method. This, however, has slightly increased the computational cost due to the incorporation of the KBC-ELB. Fortunately, the ULBM framework allows easy switch between collision operators via the relaxation matrix (***S***), so that the best choice can be made for a specific application in terms of accuracy, stability, and computational cost. The corresponding collision operators and their relaxation matrix can be found in Table I.

The shear part $(s_i)$ can be calculated by $s_i = \mathbf{M}^{-1}\mathbf{N}^{-1}\ |\tilde{\mathrm{T}}_{si}\rangle$, according to the relation $f_i = \mathbf{M}^{-1}\mathbf{N}^{-1}|\tilde{T}_i\rangle$. Based on Eq. (9), it is known the equilibrium central moments of the shear part $(|\tilde{\mathrm{T}}_{si}^{\mathrm{eq}}\rangle)$ is zero. The equilibrium state of the shear part is also zero due to $s_i^{\mathrm{eq}} = \mathbf{M}^{-1}\mathbf{N}^{-1}|\tilde{\mathrm{T}}_{si}^{\mathrm{eq}}\rangle$. Following Refs. [27,42], the deviation of the high-order part is calculated by $\Delta h_i = h_i - h_i^{\mathrm{eq}} = f_i - f_i^{\mathrm{eq}} - \Delta s_i$. It is also noted that the trace of the stress tensor $(k_{200} + k_{020} + k_{002})$ is included in the high-order part; thus, the bulk viscosity becomes $\xi = C_S^2(1/s_v\gamma - 0.5)$, depending on $s_v$ and $\gamma$ [41]. Remarkably, $|\tilde{\mathrm{T}}_i^{\mathrm{eq}}\rangle$ and $|C_i\rangle$ are explicitly given by Eqs. (9) and (12), respectively. Thus, the corresponding matrix manipulation (for the transformation to central moments) is not needed in Eq. (1). Finally, by substituting $\mathbf{M}^{-1}$, $\mathbf{N}^{-1}$, and $\mathbf{S}$ into Eq. (1), the postcollision distribution functions can be calculated by

$$\begin{aligned} f_i^* = {} & \mathbf{M}^{-1}\mathbf{N}^{-1}(\mathbf{I} - \mathbf{S})|\tilde{T}_i\rangle + \mathbf{M}^{-1}\mathbf{N}^{-1}S|\tilde{\mathrm{T}}^{\mathrm{eq}}\rangle \\ & + \mathbf{M}^{-1}\mathbf{N}^{-1}(\mathbf{I} - \mathbf{S}/2)|C_i\rangle, \end{aligned} \tag{18}$$

With the Chapman-Enskog analysis, the above ULBM with the KBC operator can reproduce the following macroscopic N-S equations in the low-Mach number limit:

$$\begin{aligned} & \partial_t \rho + \nabla \cdot (\rho \boldsymbol{u}) = 0, \\ & \partial_t(\rho \boldsymbol{u}) + \nabla \cdot (\rho \boldsymbol{u}\boldsymbol{u}) = -\nabla\left(\rho c_s^2\right) + \nabla \cdot [\rho\nu(\nabla \boldsymbol{u} + (\nabla \boldsymbol{u})^{\mathrm{T}}) \\ & \qquad + \rho(\xi - 2\nu/3)(\nabla \cdot \boldsymbol{u})\mathbf{I}] + \mathbf{F}, \end{aligned} \tag{19}$$

and the macroscopic variables can be expressed as

$$\rho = \sum_i f_i, \ \ \rho \boldsymbol{u} = \sum_i f_i \boldsymbol{e_i} + \frac{\Delta t \boldsymbol{F}}{2}, \tag{20}$$

where $\rho$ and $\boldsymbol{u}$ are density and macroscopic velocity of the fluid, respectively. In addition to the above D3Q27 model, a D3Q19 nonorthogonal moment-based KBC model is also incorporated into ULBM for comparison, and the details can be found in the Appendix.

### B. An extended combined pseudopotential model

In this study, we use the pseudopotential LB model to simulate the multiphase flow. In this model, the interaction force between the liquid and gas phases can be described by a local-neighbor ($\boldsymbol{F}_{\mathbf{int\_}L}$) form pseudopotential force [18]:

$$\boldsymbol{F}_{\mathbf{int\_}L} = -G\psi(\boldsymbol{x})\sum_i w(|\boldsymbol{e}_i|^2)\psi(\boldsymbol{x}+\boldsymbol{e}_i)\boldsymbol{e}_i, \tag{21}$$

where $\psi$ is the density-dependent pseudopotential. Besides, another neighbor-neighbor form pseudopotential force ($\boldsymbol{F}_{\mathbf{int\_}N}$) which is only determined by the neighbor information can be written as [43]

$$\boldsymbol{F}_{\mathbf{int\_}N} = -G\sum_i w(|\boldsymbol{e}_i|^2)\psi^2(\boldsymbol{x}+\boldsymbol{e}_i)\boldsymbol{e}_i, \tag{22}$$

where $G=-1$ is the interaction strength, the weights are $w(|\boldsymbol{e_i}|^2)=\omega(|\boldsymbol{e_i}|^2)/c_s^2$, and $\omega(0)=8/27$, $\omega(1)=2/27$, $\omega(2)=1/54$, and $\omega(3)=1/216$ for the D3Q27 model. The square-root form pseudopotential $\psi$ is used in this work, i.e.,

$$\psi = \sqrt{\frac{2\left(P_{\mathrm{EOS}}-\rho c_s^2\right)}{Gc^2}}, \tag{23}$$

where $c=1$ is the lattice constant and $P_{\mathrm{EOS}}$ is the pressure calculated by the equation of state (EOS). To realize large density ratio in multiphase flow for isothermal condition, we adopt the piecewise linear form EOS proposed in Ref. [44]:

$$P_{\mathrm{EOS}}(\rho) = \begin{cases} \rho\theta_g,\ \rho<\rho_1 \\ \rho_1\theta_g+(\rho-\rho_1)\theta_m,\ \rho_1<\rho<\rho_2 \\ \rho_1\theta_g+(\rho_2-\rho_1)\theta_m+(\rho-\rho_2)\theta_m,\ \rho_2<\rho \end{cases}, \tag{24}$$

where $\rho_1$ and $\rho_2$ are defined as the spinodal points, which can be achieved by solving the following equations:

$$\int_{\rho_g}^{\rho_l}\left[(\rho_1-\rho_g)\theta_g+(\rho_2-\rho_1)\theta_m+(\rho_l-\rho_2)\theta_l\right]=0,$$
$$\int_{\rho_g}^{\rho_l}\frac{1}{\rho}dP=\log\left(\frac{\rho_1}{\rho_g}\right)\theta_g+\log\left(\frac{\rho_2}{\rho_1}\right)\theta_m+\log\left(\frac{\rho_l}{\rho_2}\right)\theta_l=0, \tag{25}$$

where $\rho_l$ and $\rho_g$ are the coexistence density of the liquid phase and gas phase, respectively. The adjustable parameters $\theta_g$, $\theta_m$, and $\theta_l$ are defined as the slopes in different phase regions. The detailed discussion regarding the influence of those adjustable parameters can be found in Ref. [45]. In the following simulations, we set $\rho_l=1$ and $\rho_g=0.001$ to match the realistic water-air density ratio. $\theta_g$, $\theta_m$, and $\theta_l$ are set as 1/6, −1/120, and 1/3, respectively. The corresponding densities are:$\rho_1=0.001\,325$ and $\rho_2=0.9758$. This setup leads to the interface thickness of approximately 5 lattice spacings between the liquid phase and the gas phase.

Recently, an alternative pseudopotential lattice Boltzmann model was proposed by Kharmiani *et al.* [33], which promises to achieve large density ratio and independently adjustable surface tension. In their model, two additional terms were added to the pseudopotential force:

$$\boldsymbol{F}'_{\mathrm{int}} = \boldsymbol{F}_{\mathbf{int\_}L} - k\frac{Gc^4}{6}\nabla^2\psi\nabla\psi + (k+\lambda)\frac{Gc^4}{12}\nabla(|\nabla\psi|^2), \tag{26}$$

where $|\nabla\psi|^2=(\partial\psi/\partial x)^2+(\partial\psi/\partial y)^2+(\partial\psi/\partial z)^2$. The first-order and second-order derivatives in Eq. (26) are calculated by the lattice-based finite-difference scheme:

$$\frac{\partial\psi}{\partial x_\alpha}=\sum_i w(|\boldsymbol{e}_i|^2)\psi(\boldsymbol{x}+\boldsymbol{e}_i)\boldsymbol{e}_i,$$
$$\nabla^2\psi=2\sum_i w(|\boldsymbol{e}_i|^2)(\psi(\boldsymbol{x}+\boldsymbol{e}_i)-\psi(\boldsymbol{x})), \tag{27}$$

As pointed out in Ref. [33], the second term on the right-hand side of Eq. (26) is used to tune the surface tension. The third term is adopted to adjust the thermodynamic consistency, where the $k$-related part is for offsetting the additional high-order effect by the second term. According to the pressure tensor analysis, the thermodynamic consistency can be adjusted by the parameter $\lambda$ and the surface tension is linearly related to the parameter $k$. Because this model directly modifies the interaction force, it is more compatible with various forcing schemes and collision operators compared with the approaches of adding additional source terms to achieve thermodynamic consistency and tunable surface tension [21,24]. This flexibility makes the model very suitable for the ULBM. However, one drawback of this model is that it needs information at $\boldsymbol{x}+2\Delta x$ to calculate the last term in Eq. (26), which leads to more complexity in boundary implementation [45] and potentially reduced parallel efficiency. In this study, we improve Kharmiani's model by replacing the second layer-dependent term on the right-hand side of Eq. (26) with a modified combined-pseudopotential force:

$$\boldsymbol{F}''_{\mathrm{int}} = \tilde{\boldsymbol{F}}_{\mathbf{int}} - k\frac{Gc^4}{6}\nabla^2\psi\nabla\psi, \tag{28}$$

where the modified combined pseudopotential force ($\tilde{\boldsymbol{F}}_{\mathbf{int}}$) is written as

$$\tilde{\boldsymbol{F}}_{\mathbf{int}} = -\left(\frac{\lambda}{2}-\frac{k}{6}\right)G\sum_i w(|\boldsymbol{e}_i|^2)\psi^2(\boldsymbol{x}+\boldsymbol{e}_i)\boldsymbol{e}_i$$
$$-\left(1-\lambda+\frac{k}{3}\right)G\psi(\boldsymbol{x})\sum_i w(|\boldsymbol{e}_i|^2)\psi(\boldsymbol{x}+\boldsymbol{e}_i)\boldsymbol{e}_i. \tag{29}$$

It is noted that the modified combined pseudopotential force ($\tilde{\boldsymbol{F}}_{\mathbf{int}}$) is achieved by combining the local-neighbor and neighbor-neighbor form pseudopotential forces, inspired by Kupershtokh *et al.* [28]. The prefactor $A$ in the original combined pseudopotential force (e.g., in Refs. [28,46]) has been modified as $\lambda-k/3$. In other words, in this study, we extend the traditional combined pseudopotential model to an extended combined pseudopotential (ECP, Eq. (28)) model by adding an additional term to achieve the tunable surface

tension. Following Shan's approach [47], the discrete form pressure tensor for the pseudopotential force can be written as

$$\int (\nabla \cdot \boldsymbol{P}) d\Omega = \int \nabla \cdot \left(\rho C_S^2 \boldsymbol{I}\right) d\Omega - \int \boldsymbol{F} d\Omega, \tag{30}$$

where $d\Omega$ represents the finite volume. The discrete form pressure tensor for the modified combined-pseudopotential force [Eq. (29)] has been analyzed in Ref. [46] and can be written as

$$\tilde{\boldsymbol{P}} = \left(\rho c_s^2 + \frac{Gc^2}{2}\psi^2 + \frac{Gc^4}{12}\psi\nabla^2\psi + \left(\lambda - \frac{k}{3}\right)\frac{Gc^4}{12}|\nabla\psi|^2\right)\boldsymbol{I} + \frac{Gc^4}{6}\psi\boldsymbol{\nabla}\boldsymbol{\nabla}\psi + \left(\lambda - \frac{k}{3}\right)\frac{Gc^4}{6}\boldsymbol{\nabla}\psi\boldsymbol{\nabla}\psi. \tag{31}$$

Since $\nabla^2\psi\boldsymbol{\nabla}\psi = \boldsymbol{\nabla}(\boldsymbol{\nabla}\psi\boldsymbol{\nabla}\psi) - \boldsymbol{\nabla}|\nabla\psi|^2/2$, by expanding the last term of Eq. (28) into pressure tensor [Eq. (31)] by Shan's approach, the discrete form pressure tensor for the ECP model [Eq. (31)] can be written as

$$\boldsymbol{P''} = \left(\rho c_s^2 + \frac{Gc^2}{2}\psi^2 + \frac{Gc^4}{12}\psi\nabla^2\psi + \left(\lambda - \frac{4k}{3}\right)\frac{Gc^4}{12}|\nabla\psi|^2\right)\boldsymbol{I} + \frac{Gc^4}{6}\psi\boldsymbol{\nabla}\boldsymbol{\nabla}\psi + \left(\lambda + \frac{2k}{3}\right)\frac{Gc^4}{6}\boldsymbol{\nabla}\psi\boldsymbol{\nabla}\psi. \tag{32}$$

It should be mentioned that the surface tension relates to the term $\boldsymbol{\nabla}\psi\boldsymbol{\nabla}\psi$ and the thermodynamic consistency is influenced by the term $|\nabla\psi|^2$, which indicates the parameters $\lambda$ and $k$ can be used to adjust the thermodynamic consistency and the surface tension, respectively. Next, a one-dimensional analysis is conducted to clarify the effects of those two parameters. For the one-dimensional flat interface, the normal pressure tensor can be generally written as

$$P_n = \rho c_s^2 + \frac{Gc^2}{2}\psi^2 + \frac{Gc^4}{12}\left[a\left(\frac{d\psi}{dn}\right)^2 + b\psi\frac{d^2\psi}{dn^2}\right], \tag{33}$$

where $n$ represents the normal direction, and the prefactors $a$ and $b$ depend on the discrete gradient operator in the pseudopotential force. To satisfy the thermodynamic consistency, the liquid and gas densities should follow the relation [24]

$$\int_{\rho_g}^{\rho_l}\left(P_0 - \rho C_S^2 - \frac{Gc^2}{2}\psi^2\right)\frac{\psi'}{\psi^{1+\epsilon}}d\rho = 0, \tag{34}$$

where $\epsilon = -2a/b$. It is noted that the thermodynamic consistency is determined by the parameter $\epsilon$, and it has been pointed out that $\epsilon$ is given by $\epsilon = 0$ for the local-neighbor pseudopotential force in Eq. (21) and $\epsilon = 1$ for the neighbor-neighbor pseudopotential force in Eq. (23) [20,46]. Usually, the solution given by the thermodynamic consistency is limited to $\epsilon \in (1, 2)$ [20]. By expanding Eq. (32) for the one-dimensional flat interface, the normal pressure tensor can be written as

$$P_n'' = \rho c_s^2 + \frac{Gc^2}{2}\psi^2 + \frac{Gc^4}{12}\left[3\lambda\left(\frac{d\psi}{dn}\right)^2 + 3\psi\frac{d^2\psi}{dn^2}\right]. \tag{35}$$

Thus, in our model, $\epsilon = -2a/b = -2\lambda$. It is noted that the thermodynamic consistency is only related to the parameter $\lambda$. In other words, the parameter $k$ will not change the thermodynamic consistency and therefore our model can tune the surface tension independently of density ratio. Considering the flat interface normal to the $x$ direction, the pressure tensor components in the normal direction ($P_{xx}''$) and parallel direction ($P_{yy}''$) can be written as

$$P_{xx}'' = \rho c_s^2 + \frac{Gc^2}{2}\psi^2 + \frac{Gc^4}{12}\left[(3\lambda)\left(\frac{d\psi}{dx}\right)^2 + 3\psi\frac{d^2\psi}{dx^2}\right],$$
$$P_{yy}'' = \rho c_s^2 + \frac{Gc^2}{2}\psi^2 + \frac{Gc^4}{12}\left[\left(\lambda - \frac{4k}{3}\right)\left(\frac{d\psi}{dx}\right)^2 + \psi\frac{d^2\psi}{dx^2}\right]. \tag{36}$$

Thus, the surface tension can be expressed as

$$\sigma = \int_{-\infty}^{+\infty}(P_{xx}'' - P_{yy}'')dx = \frac{Gc^4}{6}\int_{-\infty}^{+\infty}\left[\left(\lambda + \frac{2k}{3}\right)\left(\frac{d\psi}{dx}\right)^2 + \psi\frac{d^2\psi}{dx^2}\right]dx. \tag{37}$$

Substituting the relation $\int_{-\infty}^{+\infty}\psi\frac{d^2\psi}{dx^2}dx = \psi\frac{d\psi}{dx}|_{-\infty}^{+\infty} - \int_{-\infty}^{+\infty}\frac{d\psi}{dx}d\psi$, $\frac{d\psi}{dx} = 0$ at $\pm\infty$, and $\frac{d\psi}{dx} = \frac{d\psi}{d\rho}\frac{d\rho}{dx} = \psi'\frac{d\rho}{dx}$, Eq. (37) can be simplified as

$$\sigma = -\left(1 - \lambda - \frac{2k}{3}\right)\frac{Gc^4}{6}\int_{-\infty}^{+\infty}(\psi')^2\frac{d\rho}{dx}d\rho. \tag{38}$$

According to Eq. (38), as long as $\lambda$ is fixed, the surface tension decreases linearly with the increase of $k$. The theoretical surface tension ratio is determined by

$$\frac{\sigma(k)}{\sigma(0)} = \frac{\left(1 - \lambda - \frac{2k}{3}\right)}{1 - \lambda}. \tag{39}$$

We will validate this relation in the following section. The above ULBM has been implemented in the in-house software suite UCLBM (Unified Cascaded Lattice Boltzmann Method). The following results are obtained by running the UCLBM on the UK national supercomputer ARCHER2.

## III. RESULTS AND DISCUSSION

### A. Model validation and assessment

The spurious velocity is usually regarded as the main factor that affects the numerical stability for the pseudopotential lattice Boltzmann model. In this section, we use a static droplet test to evaluate the spurious velocities of the current models. Firstly, a spherical droplet of the initial radius $R_0 = 40$ is located at the center of a $4R_0 \times 4R_0 \times 4R_0$ box. The initial density profile can be described by the following function:

$$\rho(r) = \frac{\rho_l + \rho_g}{2} + \frac{\rho_l - \rho_g}{2}\tanh\left[\frac{2(r - R_0)}{W}\right], \tag{40}$$

where $W = 5$ is the approximate interface thickness by adopting the setup in Sec. II B, and $r$ represents the distance to the droplet center. Additionally, we set the kinematic viscosity ratio between the gas phase ($\nu_g$) and liquid phase ($\nu_l$) as 10, which leads to the dynamic viscosity ratio

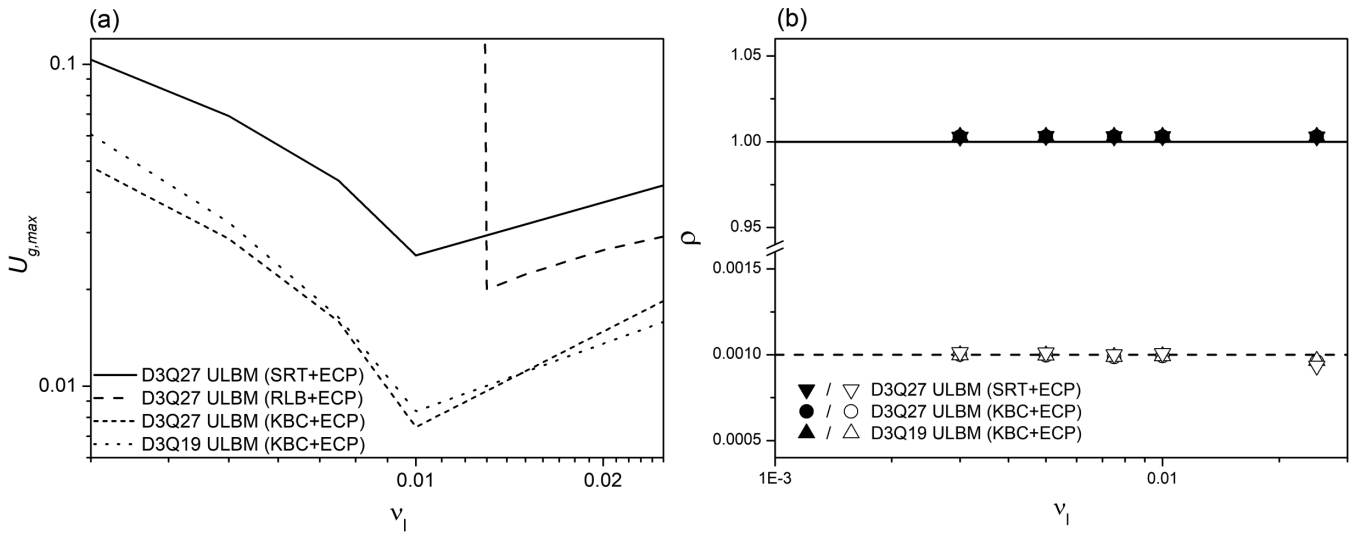


FIG. 1. (a) The maximum spurious velocities in the gas phase as a function of the liquid kinematic viscosities, at density ratio of 1000 and dynamic viscosity ratio of 100. (b) The evolution of the simulated liquid density (solid symbols) and gas density (hollow symbols) as a function of liquid viscosities. Results are for the D3Q27 ULBM (SRT+ECP), D3Q19 ULBM (KBC+ECP), and D3Q27 ULBM (KBC+ECP). The solid line and dashed line represent the theoretical liquid and gas density, respectively.

$\mu_l/\mu_v = (\rho_l \nu_l)/(\rho_v \nu_g) \approx 100$. $\lambda$ equals $-0.695$, and $\epsilon \approx 1.4$. The following interpolation is used for calculating the kinematic viscosity at the liquid-gas interface:

$$\nu = \nu_g + (\nu_l - \nu_g)\frac{\rho - \rho_g}{\rho_l - \rho_g}. \tag{41}$$

To evaluate the spurious velocities, we fix $k = 0$ and change the kinematic viscosity of the liquid phase from 0.003 to 0.025, while keeping all the other parameters the same. In order to eliminate the influence of the bulk viscosity and free parameters, four different collision operators without free parameters are tested within the same ULBM framework, that is, D3Q27 ULBM (SRT+ECP), D3Q27 ULBM (RLB+ECP) model, D3Q27 ULBM (KBC+ECP) model and D3Q19 ULBM (KBC+ECP). Figure 1(a) presents the maximum spurious velocities ($U_{g,\max}$) versus various liquid kinematic viscosities. As indicated in the figure, the D3Q27 ULBM (KBC+ECP) model and the D3Q19 ULBM (KBC+ECP) model possess similar numerical stability and outperform the ULBM (SRT+ECP) by producing 2 to 3 times lower $U_{g,\max}$. It is also found that the standard regularized LB (RLB) model [48] is less stable than the ULBM (SRT+ECP) model, which leads to numerical divergency when $\nu_l < 0.0125$. This finding agrees with the results in the study of the single-phase KBC model [41]. So, we exclude the ULBM (RLB+ECP) model in the following simulation. The results show that the present ECP model makes all the collision operators, including SRT, stable at a low liquid kinematic viscosity ($\sim 3 \times 10^{-3}$), even though the advantage of KBC over SRT models in terms of reduced spurious velocities is still significant.

The measured densities in the liquid and gas phases versus different $\nu_l$ are shown in Fig. 1(b). The simulated coexistence densities almost coincide (solid symbols stand for the liquid-phase densities and hollow symbols indicate the gas-phase densities) with the theoretical coexistence densities ($\rho_l = 1$ by the solid line and $\rho_g = 0.001$ by the dashed line). When $\nu_l$ varies from 0.003 to 0.025, for all three collision operators with the ECP model, the maximum discrepancy between the measured and theoretical densities is 7%, (at the $\nu_l = 0.025$) for the ULBM (SRT+ECP), and lower than 4% for the ULBM (KBC+ECP). The present results show that the ECP model is able to simulate the large density ratio ($\sim$1000) multiphase flow, implying a good thermodynamic consistency. It should also be mentioned that the D3Q27 ULBM (KBC+ECP) only costs around 19% additional computational time than the D3Q27 ULBM (SRT+ECP) model, which is due to the calculation of the entropic stabilizer. In contrast, the D3Q19 ULBM (KBC+ECP) spends 28% less computational time than the D3Q27 ULBM (SRT+ECP) model. It is noticed that the additional computational cost for the current ULBM (KBC+ECP) model is far less than the traditional KBC model ($\sim$2 times of computational time compared with SRT [41]). This is because the nonorthogonal moment set used in this work produces less nonzero terms in the transformation matrix $\mathbf{M}$ and its inverse matrix $\mathbf{M}^{-1}$, leading to better numerical efficiency [35].

The density contour and velocity vectors (with a fixed scale to the velocity magnitude) on the symmetry plane for selected cases are shown in Figs. 2(a)–2(d). It can be seen that, compared with the D3Q27 ULBM (SRT+ECP), the D3Q27 ULBM (KBC+ECP) considerably decreases the spurious velocities in the gas phase [see Figs. 2(a) and 2(b)]. Besides, the spurious velocities are significantly increased when $\nu_g$ is decreased [see Figs. 2(c) and 2(d)] However, the decrease of $\nu_l$ just slightly influences the spurious velocities [see Figs. 2(a) and 2(c)]. The distribution of the entropic stabilizer ($\gamma$) in the gas phase on the symmetry plane is shown in Fig. 2(e). It can be seen that $\gamma$ self-adapts around the liquid-gas interface to stabilize the simulation, which is similar to the results in Ref. [49].

Another comparison is conducted between the ECP model and the previous force model proposed by Li *et al.* [24] for large density ratio and thermodynamic consistency. The same

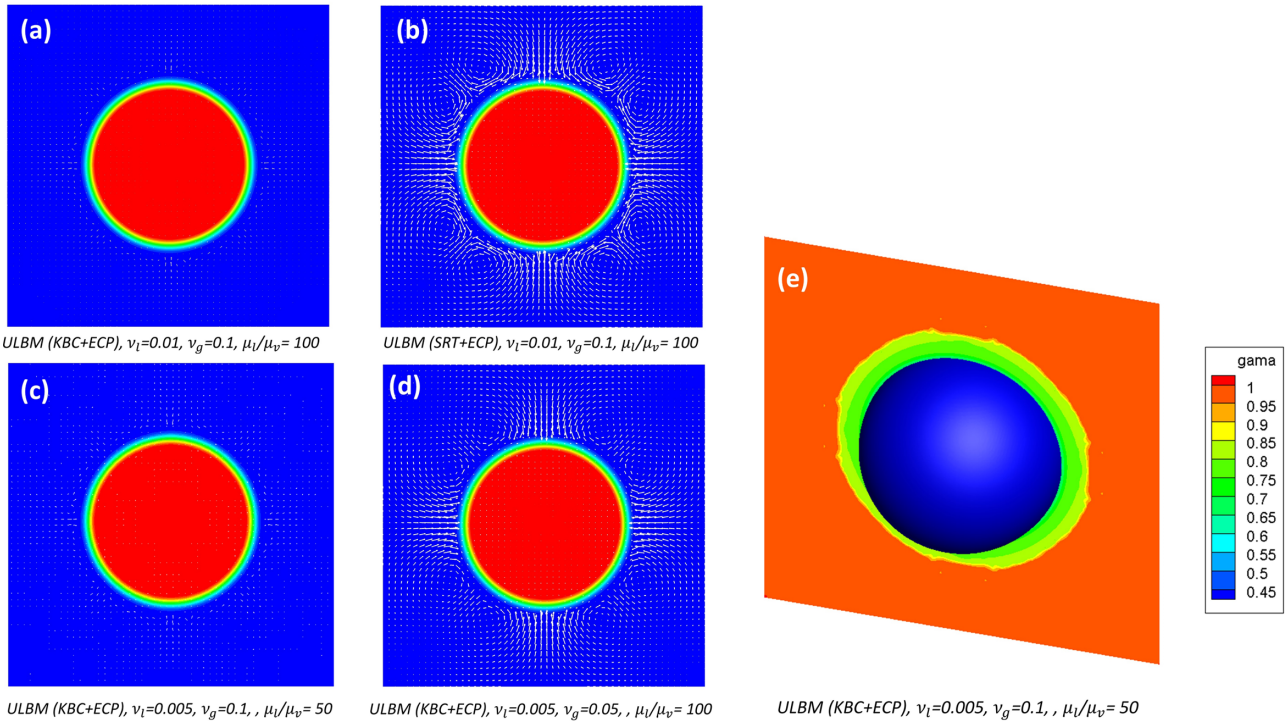


FIG. 2. (a)–(d) Density contour and velocity vectors on the symmetry plane of the simulation domain; (e) 3D droplet interface and the entropic stabilizer distribution on the symmetry plane.

static droplet is simulated. In this simulation, the ULBM (SRT) collision operator is used, and $\epsilon \approx 1.4$, $\mu_l/\mu_v = \rho_l/\rho_v \approx 1000$ for both models. The kinematic viscosity is varied from 0.018 to 0.25; the simulation results for the ECP model and Li *et al.*'s model are shown in Table II. The ECP model leads to a lower $U_{g,\max}$ for a wide range of values for the kinematic viscosity compared with Li *et al.*'s model. Also, the ECP model significantly decreases the discrepancies from the theoretical coexistence density in gas phase ($e_{\text{gas}}$) when $\nu_g > 0.15$. Considering the present ECP model equals to the original combined pseudopotential force model in Refs. [28,46] when $k = 0$, this finding also agrees with the result in Ref. [46].

We then conduct a test of the surface tension adjustment capability. Similarly, a static droplet is fixed at the center of a $4R_0 \times 4R_0 \times 4R_0$ box, $\nu_l$ is kept at 0.01, and the dynamic viscosity ratio between the liquid and gas phases is 100 at the density ratio of 1000. To verify the accuracy of the theoretical prediction in Eq. (39), we simulate a static droplet with an initial radius $R_0 = 40$, $\lambda = -0.695$ and increase $k$ from 0 to 2.4 by using the D3Q27 ULBM (KBC-ECP), D3Q19 ULBM (KBC-ECP), and D3Q27 ULBM (SRT-ECP) collision operators. The surface tension is calculated by Laplace's law $\Delta P = P_{\text{liquid}} - P_{\text{vapour}} = 2\sigma/R_0$, and the results are compared with the theoretical prediction in Eq. (39). As shown in Fig. 3(a), the simulation results obtained by various collision operators are consistent with the theoretical equation. The maximum relative error between the theoretical equation and measured results is around 5%, occurring at $k = 2.4$ ($\sigma \approx 0.001$), where $\sigma$ ($k$) has been reduced to 5% of its original value ($k = 0$, $\sigma \approx 0.02$). The simulation results prove the correctness of the theoretical analysis in Sec. II B and show our ECP model can adjust the surface tension independently of the collision operator.

We further verify Laplace's law by changing $1/R_0$ from 0.02 to 0.04 with three different tunable parameters, $k =$ [0, 1.5, 2.4], by using D3Q27 ULBM (KBC) collision operator, with all other setups being kept the same. As indicated

TABLE II. Comparison of the present ECP model and Li *et al.*'s model in a static droplet test using ULBM (SRT).

| | Li *et al.*'s model [24] | | | ECP model | | |
|---|---|---|---|---|---|---|
| $\nu_g$ | $\rho_{v_{\text{sim}}}$ | $e_{\text{gas}}$ (%) | $U_{g,\max}$ | $\rho_{v_{\text{sim}}}$ | $e_{\text{gas}}$ (%) | $U_{g,\max}$ |
| 0.25 | 0.000 829 | 20.63 | 0.114 994 | 0.000 932 | 7.32 | 0.044 457 |
| 0.15 | 0.000 929 | 7.64 | 0.046 111 | 0.000 982 | 1.85 | 0.018 453 |
| 0.05 | 0.000 994 | 0.60 | 0.069 355 | 0.001 015 | 1.45 | 0.070 567 |
| 0.025 | 0.001 005 | 0.50 | 0.128 453 | 0.001 016 | 1.57 | 0.114 487 |
| 0.018 | 0.001 012 | 1.14 | 0.172 087 | 0.001 018 | 1.76 | 0.132 782 |

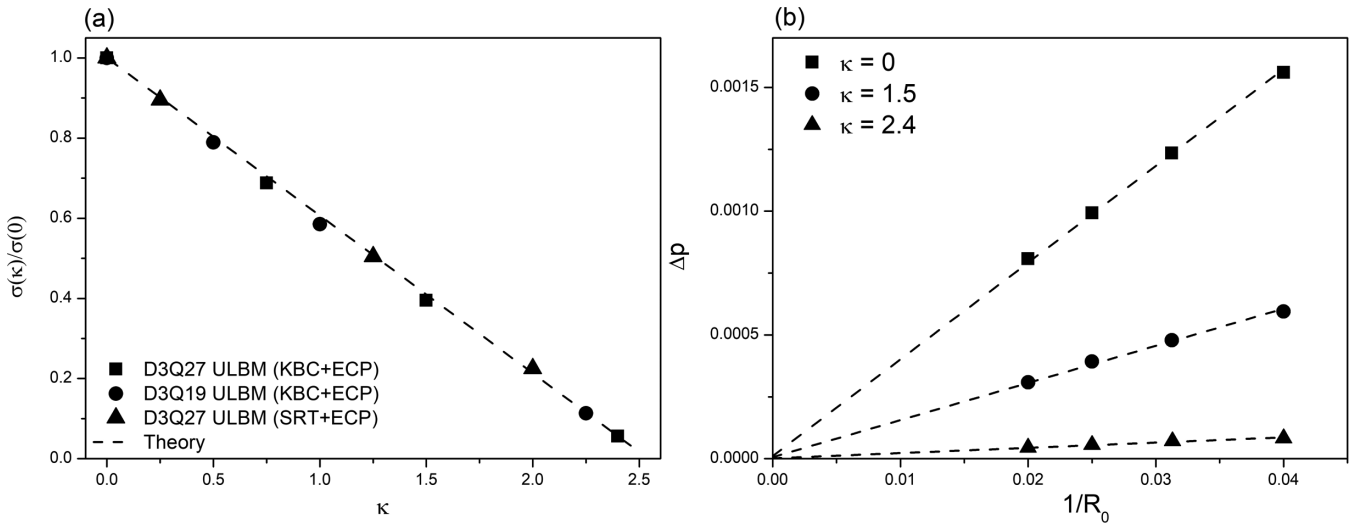


FIG. 3. (a) The evolution of the surface tension ratio for various $k$. The different symbols represent the various models, and the dashed line indicates the theoretical prediction in Eq. (39). (b) The Laplace law verification for a static droplet, where the different symbols stand for different $k$ and the dashed lines are the best-fitted lines.

in Fig. 3(b), the measured pressure differences between the liquid and gas phases ($\Delta P$) linearly increase with $1/R_0$, which concurs with Laplace's law. The maximum deviation between the measured pressure difference and its theoretical prediction is 7%, which occurs at the case with the lowest surface tension and the largest curvature ($k = 2.4$ and $1/R_0 = 0.04$). For all the other cases, the differences are lower than 5.5%.

Finally, we test the evolutions of the measured density versus the reduced surface tension $[\sigma(k)/\sigma(0)]$. The same cases in Fig. 3(a) are considered. Besides, we also test the density evolution by using Li *et al.*'s models with D3Q27 ULBM (SRT) collision operator [21,24]. In the simulations, $\epsilon$ is set as 1.4, and all other parameters are set the same for all models. As shown in Fig. 4, both our model and Li *et al.*'s model achieve a good degree of density ratio constancy for a wide range of tunable surface tension. Also, our ECP model with various collision operators presents a similar density consistency. It should be pointed out that Li *et al.*'s model becomes unstable when $\sigma(k)/\sigma(0)$ is lower than 0.25 by using the ULBM (SRT) collision operator. However, our model can stay stable when $\sigma(k)/\sigma(0) \approx 0.1$ for the same condition. The discrepancies of the gas-phase densities from its coexistence densities are lower than 5% for our ECP force model with all the collision operators.

### B. Implementation of contact angles

Droplet impingement on hydrophobic or hydrophilic surfaces is a ubiquitous multiphase phenomenon in engineering, material science, and medical science [3]. In this section, we adopt the D3Q27 ULBM (KBC+ECP) model to simulate the droplet impingement phenomenon. We add the following additional term into the forcing field ($\boldsymbol{F} = \boldsymbol{F}''_{\text{int}} + \boldsymbol{F}_{\text{ads}}$) to achieve the tunable contact angle [50]:

$$\boldsymbol{F}_{\text{ads}} = -G_w \psi(\boldsymbol{x}) \sum_i w(|\boldsymbol{e}_i|^2) \psi(\boldsymbol{x}) s(\boldsymbol{x} + \boldsymbol{e}_i \Delta t) \boldsymbol{e}_i, \quad (42)$$

where $G_w$ is the fluid-solid interaction strength to adjust the droplet contact angle. $s(\boldsymbol{x})$ is an indicator function which is equal to 1 for solid and 0 for fluid, respectively. The effect of the contact-angle hysteresis has been ignored owing to the strong hydrophobic characteristic in the following simulations. The additional contact-angle treatment such as the geometric formulation [51,52] should be considered when the three-phase contact-line motion is dominant. It should be pointed out that the local fluid density method is used to treat the unknown interaction force between the boundary fluid and solid wall. The density-dependent pseudopotential at the first layer of the solid wall [see the red dots in Fig. 8(a)] is copied

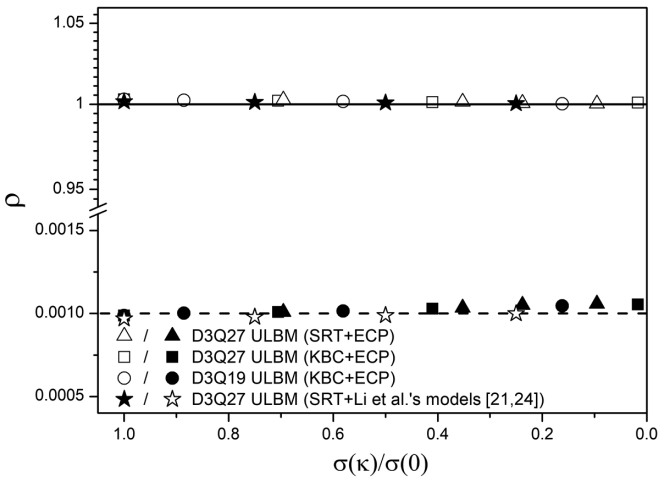


FIG. 4. The evolution of the simulated liquid density (solid symbols for ECP model and hollow symbols for Li *et al.*'s models) and gas density (hollow symbols for ECP model and solid symbols for Li *et al.*'s models) as a function of reduced surface tension, at $\rho_l/\rho_v \approx$ **1000** and $\mu_l/\mu_v = 100$. Different symbols represent various adopted models. The solid lines and dashed lines in the figures stand for the theoretical coexistence densities in the liquid and gas phases, respectively.

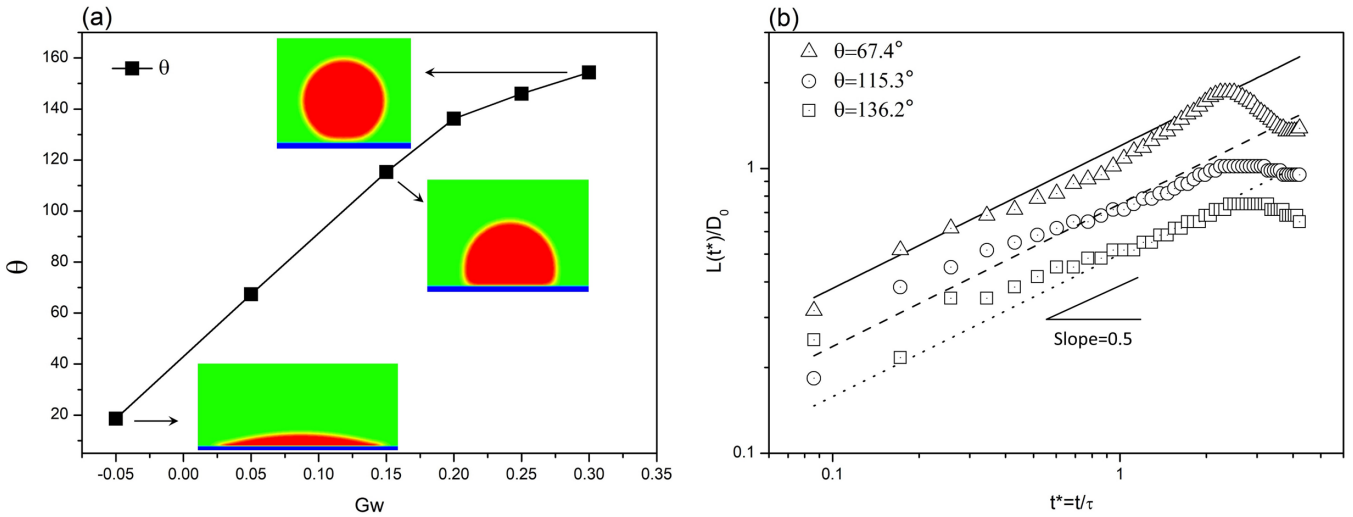


FIG. 5. (a) The droplet static contact angle vs various liquid-solid interaction strengths ($Gw$). (b) The transient evolution of the normalized contact line length for various static contact-angle cases (symbols); the lines in the figure indicate the fittings according to the theoretical relation $\mathrm{L/D_0} \sim \mathrm{t}/\tau^{0.5}$.

from the pseudopotential of the boundary fluid nodes [$\psi(\boldsymbol{X}_b)$, e.g., see the white dots in Fig. 8(a)]. One major advantage of this treatment is its simplicity in coding and dealing with complex geometries, since it does not need to specify the pseudopotential for the nodes at the solid wall. The interaction force between the boundary fluid and the solid wall can be written as

$$\boldsymbol{F}_{\mathbf{int\_solid}} = -\left(\frac{\lambda}{2}-\frac{k}{6}\right)G\sum_i w(|\boldsymbol{e}_i|^2)\psi^2(\boldsymbol{X}_b)\,\boldsymbol{e}_i - \left(1-\lambda+\frac{k}{3}\right)G\psi(\boldsymbol{X}_b)\sum_i w(|\boldsymbol{e}_i|^2)\psi(\boldsymbol{X}_b)\,\boldsymbol{e}_i, \tag{43}$$

The first verification for the contact angle is modeling the dynamic wetting process of a water droplet with an initial radius $R_0 = 30$ and $G_w$ is changed from $-0.05$ to 0.325. Figure 5(a) represents the droplet static contact angle ($\theta$) as a function of $G_w$. The static contact angle is calculated by the relation $\tan(\theta/2) = 2H/L$, where $H$ and $L$ are, respectively, the height of the spherical crown and the length of the contact line with the plate when the droplet reaches the steady state. We also record the evolution of the contact line during the wetting process. Figure 5(b) shows the variation of the contact line versus the dimensionless time [$t^* = t/\tau$, with the inertia-capillarity time $\tau = (R_0{}^3\rho_l/\gamma)^{0.5}$] for the cases at $\theta = [67.4^\circ,\ 115.3^\circ,\ 136.2^\circ]$. The data for all cases almost follow a power law $L/D_0 \sim \mathrm{t}/\tau^{0.5}$, which is consistent with the previous finding [53].

Further verifications are conducted by simulating a water droplet impacting a flat superhydrophobic surface with various Weber numbers. The D3Q27 ULBM (KBC) collision operator with the ECP model is used, and the kinematic viscosity ratio of the liquid phase and gas phase is kept at 20 and the density ratio is 1000. Besides, $R_0$ is 40 and $\nu_l$ equals 0.005, leading to an Ohnesorge number of lower than 0.006 for all simulation cases, where the Ohnesorge number is defined as $\mathrm{Oh} = (\rho_l \nu_l)/\sqrt{2R_0\rho_l\sigma}$, which stands for the relative importance of viscosity force to the mean of dynamic force and capillary force. As a result, the viscous effect can be ignored. In addition, $G_w$ is fixed at 0.32 which implies the static contact angle is over 155 °. We change the Weber number ($\mathrm{We} = 2R_0\rho_l U^2/\sigma$, where $U$ is the droplet initial velocity) from 6.4 to 120, and the corresponding Reynolds number ($\mathrm{Re} = 2R_0U/\nu_l$) varies from 640 to 1600. The simulation results are compared with the experimental results in Refs. [54,55] as well as the simulation results conducted by the traditional KBC model [49] and ELB model [30].

Figure 6(a) is the maximum spreading diameter of the droplet as a function of impacting We. As indicated in the figure, our simulation results are in line with the previous results. Additionally, the simulated maximum spreading diameter also follows a dependency of $\sim \mathrm{We}^{0.25}$, which was observed in the previous study [54]. The nondimensionalized contact time is defined as $t_{\mathrm{contact}}/\tau$, where the droplet contact time $t_{\mathrm{contact}}$ is defined as the period between the droplet first touches the solid phase and bounces from the solid phase. It has also been recorded as a function of We and plotted in Fig. 6(b). Our simulated results are compared with the experimental results in Ref. [56] and simulation results of the traditional ELB model [30]. As we can observe, our simulation results are in line with previous experimental (simulation) results. In addition, it is found that the nondimensionalized contact time is almost constant with a $t_{\mathrm{contact}}/\tau = 2.5$ dependency for all Weber numbers, which is in agreement with the finding in Ref. [55]. The good agreement between our simulation results and the theoretical results demonstrates the accuracy of the implemented contact-angle model.

### C. Simulation of realistic droplet dynamics

In this section, we adopt the D3Q27 ULBM (KBC+ECP) model to simulate droplet dynamics under realistic conditions. Benefitting from the stability of the model, the density ratio

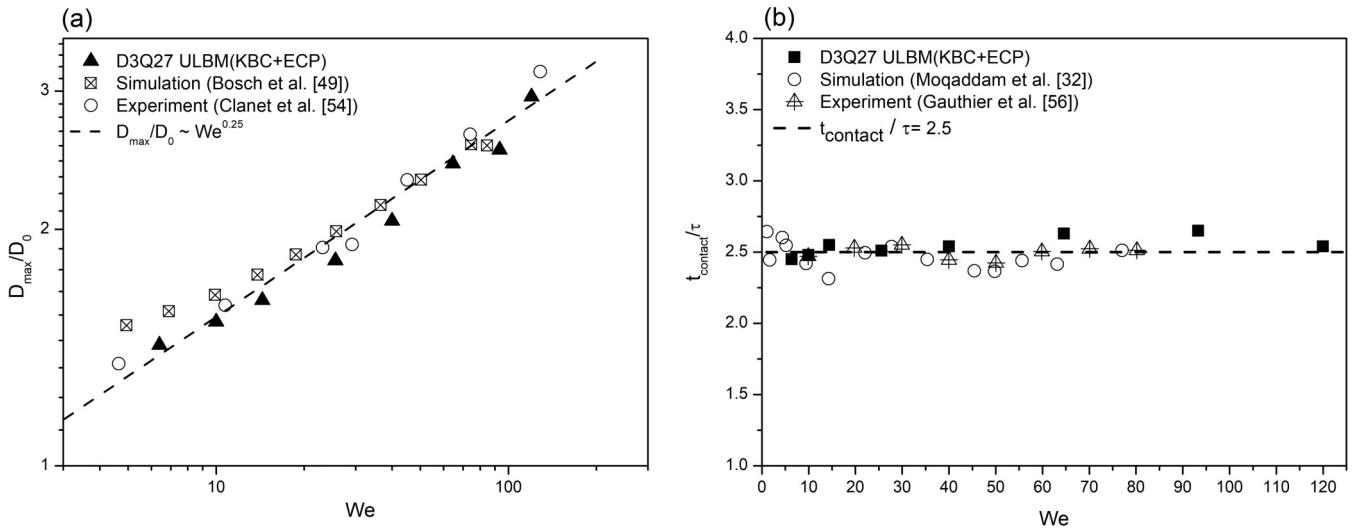


FIG. 6. A water droplet impacting a superhydrophobic plate with different We, at $\theta > 155\,^{\circ}$. (a) The normalized droplet maximum deformation diameter compared with the previous simulation results in Ref. [49], experimental results in Ref. [54], and the power-law dependency $\mathrm{D_{max}/D_0} \sim \mathrm{We}^{0.25}$. (b) The nondimensionalized contact time, compared with the simulation data in Ref. [30], the experimental data in Ref. [55], and the empirical relation $\mathbf{t_{contact}}/\boldsymbol{\tau} = 2.5$.

of the liquid phase and gas phase is set as 1000, and the kinematic viscosity of the liquid phase ($\nu_l$) is fixed at 0.004 to achieve the realistic physics parameters. We first model the binary equal size droplet collision and compare the simulation results with the experimental results in Ref. [57]. Two cases are tested: (1) Head on droplet collision at the Weber number of 40 ($\mathrm{We} = 2R_0\rho_l V^2/\sigma$, where $V = 2U$ is the relative velocity of droplets). (2) Off center droplet collision at $\mathrm{We} = 83$, and the impact factor $x = 0.4$ ($x = X/R_0$, where $X$ indicates the separation between the vertical center lines of the droplets). For both simulations, the droplet radius and kinematic viscosity ratio are fixed at 50 and 20, respectively. $k$ is kept at 0 and We is adjusted by changing the relative velocity. This setup leads the Ohnesorge number to 0.004, which is similar to the experimental parameter.

As indicated in Fig. 7, our simulation results qualitatively agree with the experimental results. For case (1) in Fig. 7(a), a liquid disk forms after the droplet collision, and reflexive separations of the two droplets are observed after the liquid disk reaches the maximum deformation diameter. Then, a liquid bridge can be observed between the two separated satellite droplets. Finally, the neck of the liquid bridge breaks up and the liquid bridge retracts to the third satellite droplet, which finally leads to reflexive separation of three satellite droplets. Regarding case (2) in Fig. 7(b), it is found that a liquid bridge occurs after two droplets collide. With two droplets continuously separating, the liquid bridge stretches and breaks. Finally, a satellite droplet is formed owing to the breakup of the liquid bridge, which finally exhibits stretching separation of three satellite droplets.

Then, we simulate a water droplet impacting superhydrophobic curved surfaces and qualitatively compare the results with the experimental results in Ref. [58]. In this simulation, $G_w$ is fixed as 0.35 and the static contact angle is around $160\,^{\circ}$. The impacting We is set as 20, which is consistent with the experimental conditions. All the other parameters are kept the same as the last simulation. Two different superhydrophobic surfaces with the normalized curve radius $R_c/R_0 = 2.3$ [Fig. 8(a)] and $R_c/R_0 = 0.4$ [Fig. 8(b)] are tested. As demonstrated in the figure, our simulation results (blue snapshots) agree well with the experimental data (gray snapshots) qualitatively. Besides, unlike the pervious LB simulation results for the same case [35,58], our present model has reproduced detailed features observed in the experiments, such as the satellite droplet in the last frame of Fig. 8(b), thanks to the low viscosity and high density ratio achieved.

### D. Simulation of complex droplet dynamics

In this section, we further test the accuracy and robustness of the improved ULBM by simulating complex droplet dynamics. The cases of droplet pancake bouncing when impacting the superhydrophobic pillar surfaces and droplet collision splashing at large Weber number and Reynolds number are reproduced. In the following simulations, the D3Q27 ULBM (KBC) collision operator and the ECP model are adopted.

#### *1. Droplet pancake bouncing*

Liu *et al.* [59] first found that a droplet experiences pancake bouncing when impacting a superhydrophobic pillar-textured surface under a moderate Weber number, and the contact time of the droplet with the surface can be significantly decreased. Some subsequent studies on this phenomenon have been conducted experimentally and numerically in recent years [30,60,61]. In the previous LBM simulation studies for this case, the adopted density ratios were far less than the real value and the viscosities were kept artificially high ($\nu_l > 0.05$) to ensure the numerical stability [30,61]. Here we simulate this phenomenon by using realistic physical parameters ($\rho_l/\rho_v = 1000$, $\mathrm{Oh} < 0.004$ with $\nu_l = 0.004$), and compare

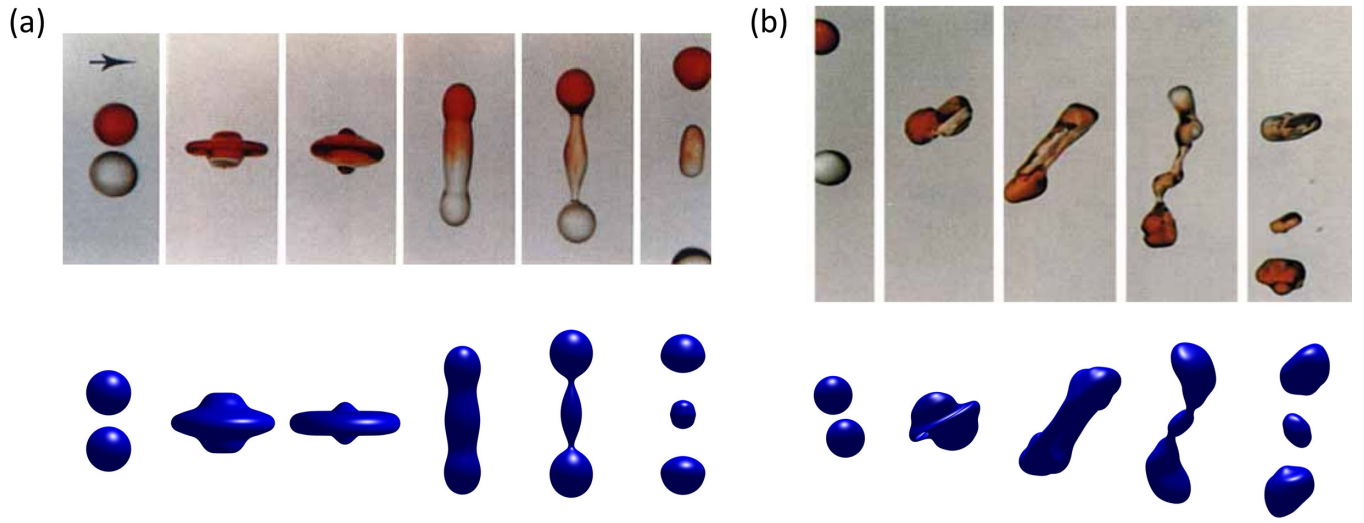


FIG. 7. A comparison of the simulation results with the experimental results for binary equal size droplet collision. The top column stands for the experimental results in Ref. [57] and the bottom column represents the present simulation results. (a) Head-on droplet collision at We = 40; (b) Off-center droplet collision at We = **8**4 and x = **0**.34.

the simulation results with the experimental data in Ref. [60]. The cases at We = 26.6, $\theta \approx 160^{\circ}$ with various intervals between the pillars are considered.

In our simulation, the initial radius of the droplet ($R_0$) is 65 in lattice units, and the simulation domain is a $6R_0 \times 6R_0 \times 4R_0$ box. The half-way bounceback boundary scheme is adopted in the solid surfaces as well as top and bottom walls, and all the other boundaries are configurated as the periodic boundary. $G_w$ is 0.35 so that the static contact angle is around 160 °. The impacting parameters for the simulations are We ≈ 27 and Re ≈ 2000 for all cases. The height ($H_P$) and diameter ($D_P$) of the pillars are 40 and 12 in lattice units, respectively. The corresponding $H_P/R_0 = 0.615$ and $D_P/R_0 = 0.18$, which are the same as the experimental conditions. The intervals ($S$) between the pillars are 20, 22, 24, and 28 in lattice units, corresponding to the intervals of 0.2, 0.25, 0.3, and 0.4 mm in the experiment, respectively.

The qualitative comparison results for the cases with the intervals of 0.2, 0.25, and 0.3 mm are shown in Figs. 9(a), 9(b) and 9(c), respectively. It can be seen that our simulation

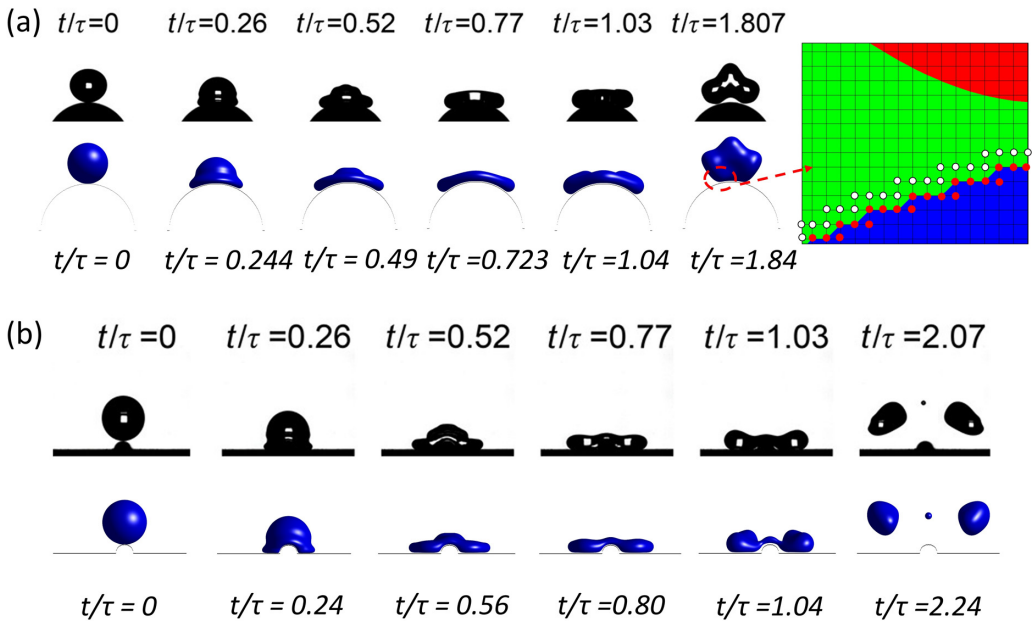


FIG. 8. Comparison between the experimental snapshots (gray) [58] and the ULBM (KBC+ECP) simulation results (blue) of a water droplet impacting curved superhydrophobic surfaces at We≈40, and $\theta > 160^{\circ}$. (a) $R_c/R_0 = 2.3$ and (b) $R_c/R_0 = 0.4$. The zoomed-in view in (a) reveals the distribution of the nodes at the first layer of the solid wall (red dots) and the boundary fluid nodes (white dots), where the blue, green, and red regions represent the solid, gas, and liquid phases, respectively.

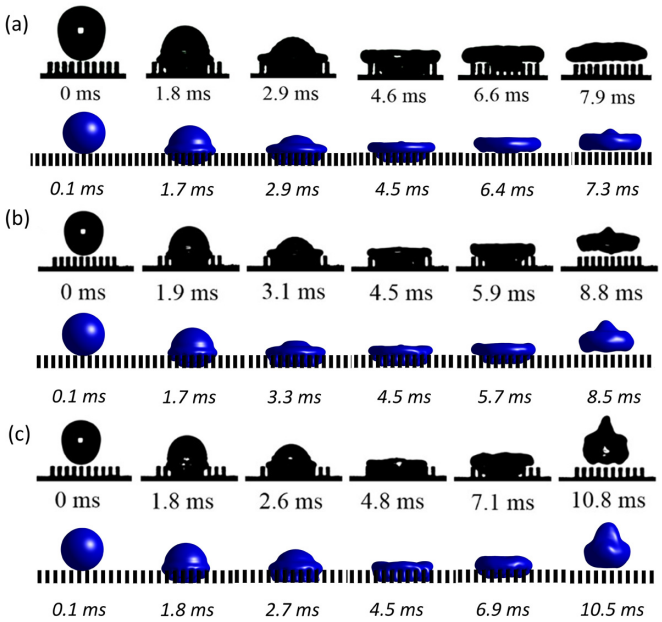


FIG. 9. Qualitative comparison between the experiment results (gray) [60] and simulation results (blue) of a water droplet ($R_0 = 1.62$ mm) impacting superhydrophobic textured surface at $We = 26.6$. The height of the pillars ($H_P$) is 1 mm, the pillar diameter ($D_P$) equals 0.3 mm, and the intervals between the pillars are (a) $S = 0.2$ mm, (b) 0.25 mm, and (c) 0.3 mm, respectively.

results (blue snapshots) have an excellent agreement with the experimental results (gray snapshots). As observed, when the droplet touches the pillar's surface, the top part of the droplet starts to spread above the pillars and the bottom part of the droplet penetrates the gaps between the pillars. Owing to the capillary resistance produced by the superhydrophobic textured surface, the spreading of the droplet top part is faster than the bottom part. In contrast, the retraction of the bottom part is earlier than the top part. Thus, it can be observed that the droplet top part is still spreading (retracting) when the bottom part fully retracts and bounces off from the pillars. Additionally, the smaller the intervals, the faster the retraction of the droplet bottom part will be. As a result, we can find the bounce-off diameter of the droplet decreases with the increase of the pillar intervals, and the bounce-off time increases with the pillar intervals.

The droplet contact time and its rebound diameter have also been recorded and compared with the experimental results quantitatively in Fig. 10. The contact time ($t_{\text{contact}}$, in left axis) is defined as the instant when the droplet leaves the pillar's surface. The rebound spreading ratio $Q$ (right axis) is calculated by the droplet diameter when it bounces off from the pillar surface divided by its initial value ($D_0$). As presented in Fig. 10, our simulation results are in line with the experimental results qualitatively. The contact time decreases with the pillar intervals; In contrast, the rebound spreading ratio $Q$ decreases with the increase of pillar intervals. The small quantitative discrepancies between the simulation and experimental results can be explained by the differences in data recording.

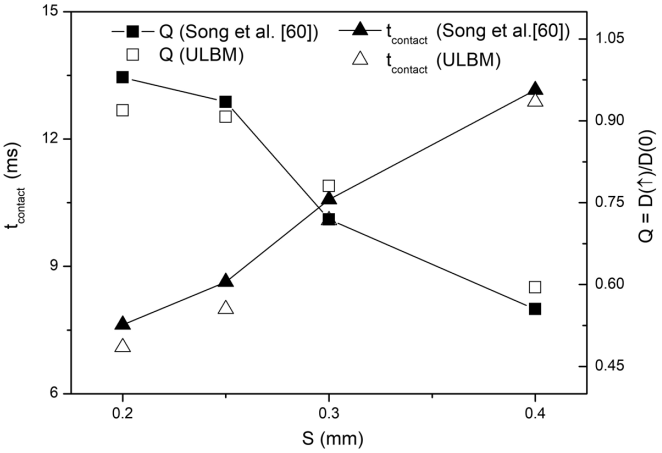


FIG. 10. Quantitative comparison of the experiment results (symbols with lines) [60] and simulation results (hollow symbols) of the droplet contact time (left axis) and Q (right axis), for the cases of a water droplet ($R_0 = 1.62$ mm) impacting the superhydrophobic pillars surface ($H_P = 1$ mm, $D_P = 0.3$ mm) with various pillar intervals ($S$) at We $\approx 27$.

### 2. *Droplet collision splashing at large Weber number and Reynolds number*

Finally, we test the ULBM (KBC+ECP) model by simulating the splashing process of the binary droplet head-on collision at large Weber number and Reynolds number. The simulation starts with the impacting Weber number ($\text{We} = 2R_0\rho_l V^2/\sigma$, where $V = 2U$ is the relative velocity of droplets) and Reynolds number ($\text{Re} = 2R_0V/\nu_l$) equal to 560 and 6000, respectively, by setting $R_0 = 60$, $k = 1.5$, $\nu_l/\nu_g = 20$, $\nu_l = 0.004$, and two droplets of equal diameter start with an equivalent initial velocity $U = 0.1$. The simulation domain is a $13R_0 \times 13R_0 \times 6R_0$ box with the periodic boundary in all directions, leading to the final grid number of over 220 million. A small random oscillation was given to the droplet initial velocity to break the symmetry. The simulation results are shown as the blue snapshots in Fig. 11.

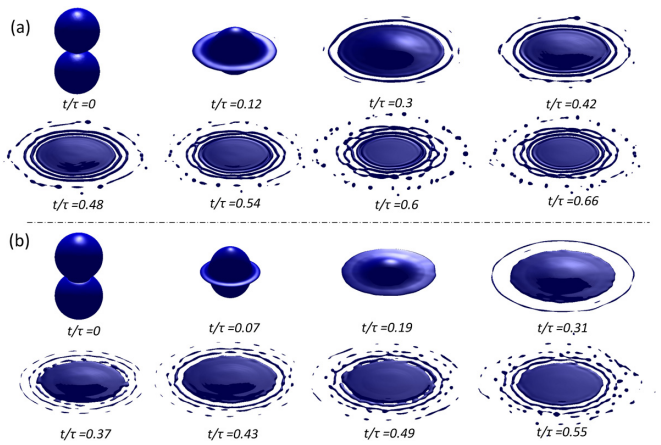


FIG. 11. Simulation of binary equal-size droplet collision at high Weber number and Reynolds number. The blue snapshots stand for the simulation results of ULBM (KBC+ECP) model. (a) We = 560, Re = 6000 and (b) We = 800, Re = 7200.

As shown in the figure, the ULBM (KBC+ECP) model is able to reproduce the splashing processes of droplet head-on collision at large Weber number and a Reynolds number. For the case with We = 560 and Re = 6000, after the droplet collision, a liquid disk forms and expands. During the liquid-disk expansion, liquid rims start to tear off from the liquid disk, which then continuously break up into many small satellite droplets. Besides, the capillary wave can be observed on the liquid disk [Fig. 11(a), from $t/\tau = 0.42$ to $t/\tau = 0.66$], which concurs with the experimental findings by Kuan *et al.* [62]. Then we increase the initial velocity to $U = 0.12$, while all the other parameters are kept the same. This setup leads to the final We = 800 and Re = 7200, respectively. The simulation results are shown in Fig. 11(b). As shown in Fig. 11(b), compared with the lower We case [Fig. 11(a)], the liquid disk spreads faster. Quantitatively, the simulated splashing processes are in line with the results reported in previous experiments and simulations [62–64]. And, this splashing simulation can prove the present LB model is capable of reproducing the key features of complex droplet dynamics at high Weber and Reynolds numbers. It should be noted that the fingering between the disk and the rims [e.g., in Fig. 11(b), from $t/\tau = 0.37$ to $t/\tau = 0.49$, occurs at the edge of the liquid disk] is successfully reproduced, which was also observed in the experiments (e.g., in Refs. [63,65]) when the Weber number is large. Such a fingering phenomenon is less obvious in the previous CLBM simulation [20] at We = 440 and Re = 6210.

## IV. CONCLUSION

In this paper, a recently developed ULBM framework is deployed to incorporate an improved collision operator and an extended combined pseudopotential model for multiphase flow simulation. Thanks to the enhanced stability, computational efficiency, and predictive capability, droplet dynamics under realistic conditions at high Weber and Reynolds numbers are reproduced. The collision operator is constructed by combining a nonorthogonal moment set with the KBC-ELB model. The ECP model is shown to be capable of high density ratio and tunable surface tension. Moreover, the resulting ULBM can reduce spurious velocities over a wide range of viscosity, while achieving good thermodynamic consistency. The extended ULBM is then applied to a variety of benchmark droplet dynamic simulations, achieving excellent agreement with the experiment data. Finally, we deploy the ULBM to more challenging cases including droplet pancake bouncing and collision splashing. Here is a summary of the key new features of the ULBM:

(1) All high-order relaxation parameters are determined by the maximum entropy condition, with no free model parameters in the collision operator.

(2) D3Q27 ULBM (KBC+ECP) and D3Q19 ULBM (KBC+ECP) can produce 2 to 3 times lower spurious velocities compared with the D3Q27 ULBM (SRT+ECP) model. The D3Q27 ULBM (KBC+ECP) consumes 19% additional computational time than the D3Q27 ULBM (SRT+ECP) model, while the D3Q19 ULBM (KBC+ECP) spends 28% less computational time than the D3Q27 ULBM (SRT+ECP) model.

(3) The ECP model is able to achieve thermodynamic consistency and adjust the surface tension almost independently of the density ratio; The variation of the gas-phase density is lower than 5% when tuning the surface tension over a wide range of values. The measured surface tension based on Laplace's law test agrees with the theoretical prediction in Eq. (39).

(4) The improved ULBM can accurately reproduce complex droplet dynamics such as droplet pancake bouncing and droplet collision splashing at Weber and Reynolds numbers up to We = 800, Re = 7200 at a density ratio of 1000.

## ACKNOWLEDGMENTS

This work was supported by the UK Engineering and Physical Sciences Research Council (EPSRC) under the project "UK Consortium on Mesoscale Engineering Sciences (UKCOMES)" (Grant No. EP/R029598/1) and the project "Exascale Computing for System-Level Engineering: Design, Optimisation and Resilience" (Grant No. EP/V001531/1).

## APPENDIX

The D3Q19 ULBM (KBC) collision operator is introduced in the Appendix. The discrete velocities of the D3Q19 lattice model are

$$\begin{aligned}
|e_{ix}\rangle &= [0, 1, -1, 0, 0, 0, 0, 1, -1, 1, -1, 1, -1, 1, -1, 0, 0, 0, 0]^{\mathrm{T}},\\
|e_{iy}\rangle &= [0, 0, 0, 1, -1, 0, 0, 1, 1, -1, -1, 0, 0, 0, 0, 1, -1, 1, -1]^{\mathrm{T}},\\
|e_{iz}\rangle &= [0, 0, 0, 0, 0, 1, -1, 0, 0, 0, 0, 1, 1, -1, -1, 1, 1, -1, -1]^{\mathrm{T}}.
\end{aligned} \tag{A1}$$

And, the D3Q19 nonorthogonal raw moment set ($|T_i\rangle$) can be written as

$$\begin{aligned}
|T_i\rangle = \mathbf{M}f_i = k_{000},\ k_{100},\ k_{010},\ k_{001},\ k_{110},\ k_{101},\ k_{011},\ k_{200}+k_{020}+k_{002},\ k_{200}-k_{020},\ k_{200}\\
-k_{002},\ k_{120},\ k_{102},\ k_{210},\ k_{201},\ k_{012},\ k_{021},\ k_{220},\ k_{202},\ k_{022}]^{\mathrm{T}},
\end{aligned} \tag{A2}$$

Thus, the transformation matrix **M** is

$$\mathbf{M} = \begin{bmatrix}
1 & 1 & 1 & 1 & 1 & 1 & 1 & 1 & 1 & 1 & 1 & 1 & 1 & 1 & 1 & 1 & 1 & 1 & 1 \\
0 & 1 & -1 & 0 & 0 & 0 & 0 & 1 & -1 & 1 & -1 & 1 & -1 & 1 & -1 & 0 & 0 & 0 & 0 \\
0 & 0 & 0 & 1 & -1 & 0 & 0 & 1 & 1 & -1 & -1 & 0 & 0 & 0 & 0 & 1 & -1 & 1 & -1 \\
0 & 0 & 0 & 0 & 0 & 1 & -1 & 0 & 0 & 0 & 0 & 1 & 1 & -1 & -1 & 1 & 1 & -1 & -1 \\
0 & 0 & 0 & 0 & 0 & 0 & 0 & 1 & -1 & -1 & 1 & 0 & 0 & 0 & 0 & 0 & 0 & 0 & 0 \\
0 & 0 & 0 & 0 & 0 & 0 & 0 & 0 & 0 & 0 & 0 & 1 & -1 & -1 & 1 & 0 & 0 & 0 & 0 \\
0 & 0 & 0 & 0 & 0 & 0 & 0 & 0 & 0 & 0 & 0 & 0 & 0 & 0 & 0 & 1 & -1 & -1 & 1 \\
0 & 1 & 1 & 1 & 1 & 1 & 1 & 2 & 2 & 2 & 2 & 2 & 2 & 2 & 2 & 2 & 2 & 2 & 2 \\
0 & 1 & 1 & -1 & -1 & 0 & 0 & 0 & 0 & 0 & 0 & 1 & 1 & 1 & 1 & -1 & -1 & -1 & -1 \\
0 & 1 & 1 & 0 & 0 & -1 & -1 & 1 & 1 & 1 & 1 & 0 & 0 & 0 & 0 & -1 & -1 & -1 & -1 \\
0 & 0 & 0 & 0 & 0 & 0 & 0 & 1 & -1 & 1 & -1 & 0 & 0 & 0 & 0 & 0 & 0 & 0 & 0 \\
0 & 0 & 0 & 0 & 0 & 0 & 0 & 0 & 0 & 0 & 0 & 1 & -1 & 1 & -1 & 0 & 0 & 0 & 0 \\
0 & 0 & 0 & 0 & 0 & 0 & 0 & 1 & 1 & -1 & -1 & 0 & 0 & 0 & 0 & 0 & 0 & 0 & 0 \\
0 & 0 & 0 & 0 & 0 & 0 & 0 & 0 & 0 & 0 & 0 & 1 & 1 & -1 & -1 & 0 & 0 & 0 & 0 \\
0 & 0 & 0 & 0 & 0 & 0 & 0 & 0 & 0 & 0 & 0 & 0 & 0 & 0 & 0 & 1 & -1 & 1 & -1 \\
0 & 0 & 0 & 0 & 0 & 0 & 0 & 0 & 0 & 0 & 0 & 0 & 0 & 0 & 0 & 1 & 1 & -1 & -1 \\
0 & 0 & 0 & 0 & 0 & 0 & 0 & 1 & 1 & 1 & 1 & 0 & 0 & 0 & 0 & 0 & 0 & 0 & 0 \\
0 & 0 & 0 & 0 & 0 & 0 & 0 & 0 & 0 & 0 & 0 & 1 & 1 & 1 & 1 & 0 & 0 & 0 & 0 \\
0 & 0 & 0 & 0 & 0 & 0 & 0 & 0 & 0 & 0 & 0 & 0 & 0 & 0 & 0 & 1 & 1 & 1 & 1
\end{bmatrix}$$

The corresponding central moment set ($|\tilde{T}_i\rangle$) and its equilibria moment set ($|\tilde{T}_i^{\mathrm{eq}}\rangle$) can be written as

$$|\tilde{T}\rangle = \mathbf{NM}f_i = [\tilde{k}_{000}, \tilde{k}_{100}, \tilde{k}_{010}, \tilde{k}_{001}, \tilde{k}_{110}, \tilde{k}_{101}, \tilde{k}_{011}, \tilde{k}_{200} + \tilde{k}_{020} + \tilde{k}_{002}, \tilde{k}_{200} - \tilde{k}_{020}, \tilde{k}_{200} - \tilde{k}_{002}, \tilde{k}_{120}, \tilde{k}_{102}, \tilde{k}_{210}, \tilde{k}_{210}, \tilde{k}_{012}, \tilde{k}_{021}, \tilde{k}_{220}, \tilde{k}_{202}, \tilde{k}_{022}]^{\mathrm{T}}, \tag{A3}$$

and

$$\left|\tilde{T}_i^{\mathrm{eq}}\right\rangle = \left[\rho, 0, 0, 0, 0, 0, 0, 3\rho C_S^2, 0, 0, 0, 0, 0, 0, 0, 0, \rho C_S^4, \rho C_S^4, \rho C_S^4\right]^{\mathrm{T}}. \tag{A4}$$

Additionally, the forcing terms in the central moment can be written as

$$|C_i\rangle = \mathbf{NM}|R_i\rangle = \left[0,\ F_x,\ F_y,\ F_z,\ 0,\ 0,\ 0,\ 0,\ 0,\ 0,\ F_x C_S^2,\ F_x C_S^2,\ F_y C_S^2,\ F_z C_S^2,\ F_y C_S^2,\ F_z C_S^2,\ 0,\ 0,\ 0\right]^{\mathrm{T}}. \tag{A5}$$

To construct the D3Q19 ULBM (KBC) model, the shear-part moment set ($|\tilde{\mathrm{T}}_{si}\rangle$) and high-order moment set ($|\tilde{\mathrm{T}}_{hi}\rangle$) in central space are

$$|\tilde{\mathrm{T}}_{si}\rangle = [0, 0, 0, 0, k_{110}, k_{101}, k_{011}, 0, k_{200} - k_{020}, k_{200} - k_{002}, 0, 0, 0, 0, 0, 0, 0, 0, 0]^{\mathrm{T}}. \tag{A6}$$

And,

$$|\tilde{\mathrm{T}}_{hi}\rangle = [0, 0, 0, 0, 0, 0, 0, 0,\ \tilde{k}_{200} + \tilde{k}_{020} + \tilde{k}_{002}, 0, 0, k_{120}, k_{102}, k_{210}, k_{201}, k_{012}, k_{021}, k_{220}, k_{202}, k_{022}]^{\mathrm{T}}. \tag{A7}$$

Finally, the relaxation parameters are

$$\mathbf{S} = \mathrm{diag}(0, 1, 1, 1, s_v, s_v, s_v, s_v\gamma, s_v, s_v, s_v\gamma, s_v\gamma, s_v\gamma, s_v\gamma, s_v\gamma, s_v\gamma, s_v\gamma, s_v\gamma, s_v\gamma). \tag{A8}$$


[1] D. Khojasteh, M. Kazerooni, S. Salarian, and R. Kamali, Droplet impact on superhydrophobic surfaces: A review of recent developments, J. Ind. Eng. Chem. **42**, 1 (2016).

[2] L. Cao, A. K. Jones, V. K. Sikka, J. Wu, and D. Gao, Anti-icing superhydrophobic coatings, Langmuir **25**, 12444 (2009).

[3] D. K. Sarkar and M. Farzaneh, Superhydrophobic coatings with reduced ice adhesion, J. Adhes. Sci. Technol. **23**, 1215 (2009).

[4] J. R. Castrejón-Pita, G. D. Martin, S. D. Hoath, and I. M. Hutchings, A simple large-scale droplet generator for studies of inkjet printing, Rev. Sci. Instrum. **79**, 075108 (2008).

[5] H. Y. Gan, X. Shan, T. Eriksson, B. K. Lok, and Y. C. Lam, Reduction of droplet volume by controlling actuating waveforms in inkjet printing for micro-pattern formation, J. Micromech. Microeng. **19**, 055010 (2009).

[6] J. Kim, Spray cooling heat transfer: The state of the art, Int. J. Heat Fluid Flow **28**, 753 (2007).

[7] Q. Li, K. H. Luo, Q. J. Kang, Y. L. He, Q. Chen, and Q. Liu, Lattice Boltzmann methods for multiphase flow and phase-change heat transfer, Prog. Energy Combust. Sci. **52**, 62 (2015).

[8] S. Succi, *The Lattice Boltzmann Equation: For Complex States of Flowing Matter* (Oxford University Press, Oxford, 2018).

[9] S. Chen and G. D. Doolen, Lattice Boltzmann method for fluid flows, Annu. Rev. Fluid Mech. **30**, 329 (1998).

[10] H. Huang, M. Sukop, and X. Lu, *Multiphase Lattice Boltzmann Methods: Theory and Application* (Wiley-Blackwell, Oxford, 2015).

[11] L. Chen, Q. Kang, Y. Mu, Y. L. He, and W. Q. Tao, A critical review of the pseudopotential multiphase lattice Boltzmann model: Methods and applications, Int. J. Heat Mass Transfer **76**, 210 (2014).

[12] G. Wang, L. Fei, and K. H. Luo, Lattice Boltzmann simulation of a water droplet penetrating a micropillar array in a microchannel, Phys. Fluids **33**, 043308 (2021).

[13] L. Fei, J. Yang, Y. Chen, H. Mo, and K. H. Luo, Mesoscopic simulation of three-dimensional pool boiling based on a phase-change cascaded lattice Boltzmann method, Phys. Fluids **32**, 103312 (2020).

[14] L. Fei, F. Qin, G. Wang, K. H. Luo, D. Derome, and J. Carmeliet, Droplet evaporation in finite-size systems: Theoretical analysis and mesoscopic modeling, Phys. Rev. E **105**, 025101 (2022).

[15] A. K. Gunstensen, D. H. Rothman, S. Zaleski, and G. Zanetti, Lattice Boltzmann model of immiscible fluids, Phys. Rev. A **43**, 4320 (1991).

[16] M. R. Swift, W. R. Osborn, and J. M. Yeomans, Lattice Boltzmann Simulation of Nonideal Fluids, Phys. Rev. Lett. **75**, 830 (1995).

[17] X. He, S. Chen, and R. Zhang, A lattice Boltzmann scheme for incompressible multiphase flow and its application in simulation of Rayleigh-Taylor instability, J. Comput. Phys. **152**, 642 (1999).

[18] X. Shan and H. Chen, Lattice Boltzmann model for simulating flows with multiple phases and components, Phys. Rev. E. **47**, 1815 (1993).

[19] M. Sbragaglia, R. Benzi, L. Biferale, S. Succi, K. Sugiyama, and F. Toschi, Generalized lattice Boltzmann method with multirange pseudopotential, Phys. Rev. E **75**, 026702 (2007).

[20] Q. Li, K. H. Luo, and X. J. Li, Forcing Scheme in Pseudopotential Lattice Boltzmann Model for Multiphase Flows, Phys. Rev. E **86**, 016709 (2012).

[21] Q. Li and K. H. Luo, Achieving tunable surface tension in the pseudopotential lattice Boltzmann modeling of multiphase flows, Phys. Rev. E - Stat. Nonlinear, Soft Matter Phys. **88**, 053307 (2013).

[22] D. Lycett-Brown and K. H. Luo, Cascaded lattice Boltzmann method with improved forcing scheme for large-density-ratio multiphase flow at high Reynolds and Weber numbers, Phys. Rev. E **94**, 053313 (2016).

[23] D. Lycett-Brown and K. H. Luo, Multiphase cascaded lattice Boltzmann method, Comput. Math. Appl. **67**, 350 (2014).

[24] Q. Li, K. H. Luo, and X. J. Li, Lattice Boltzmann modeling of multiphase flows at large density ratio with an improved pseudopotential model, Phys. Rev. E - Stat. Nonlinear, Soft Matter Phys. **87**, 053307 (2013).

[25] P. Lallemand and L. S. Luo, Theory of the lattice Boltzmann method: Dispersion, dissipation, isotropy, Galilean invariance, and stability, Phys. Rev. E **61**, 6546 (2000).

[26] A. Mazloomi M., S. S. Chikatamarla, and I. V. Karlin, Entropic Lattice Boltzmann Method for Multiphase Flows, Phys. Rev. Lett. **114**, 174502 (2015).

[27] I. V. Karlin, F. Bösch, and S. S. Chikatamarla, Gibbs' principle for the lattice-kinetic theory of fluid dynamics, Phys. Rev. E - Stat. Nonlinear, Soft Matter Phys. **90**, 031302(R) (2014).

[28] A. L. Kupershtokh, D. A. Medvedev, and D. I. Karpov, On equations of state in a lattice Boltzmann method, Comput. Math. with Appl. **58**, 965 (2009).

[29] D. Lycett-Brown and K. H. Luo, Improved forcing scheme in pseudopotential lattice Boltzmann methods for multiphase flow at arbitrarily high density ratios, Phys. Rev. E - Stat. Nonlinear, Soft Matter Phys. **91**, 023305 (2015).

[30] A. Mazloomi Moqaddam, S. S. Chikatamarla, and I. V. Karlin, Drops bouncing off macro-textured superhydrophobic surfaces, J. Fluid Mech. **824**, 866 (2017).

[31] K. H. Luo, L. Fei, and G. Wang, A unified lattice Boltzmann model and application to multiphase flows, Philos. Trans. R. Soc. A: Math. Phys. Eng. Sci. **379**, 20200397 (2021).

[32] L. Fei, K. H. Luo, and Q. Li, Three-dimensional cascaded lattice Boltzmann method: Improved implementation and consistent forcing scheme, Phys. Rev. E **97**, 053309 (2018).

[33] S. F. Kharmiani, H. Niazmand, and M. Passandideh-Fard, An alternative high-density ratio pseudo-potential lattice Boltzmann model with surface tension adjustment capability, J. Stat. Phys. **175**, 47 (2019).

[34] Y. H. Qian, D. D'Humières, and P. Lallemand, Lattice BGK models for Navier-Stokes equation, EPL **17**, 479 (1992).

[35] L. Fei, J. Du, K. H. Luo, S. Succi, M. Lauricella, A. Montessori, and Q. Wang, Modeling realistic multiphase flows using a non-orthogonal multiple-relaxation-time lattice Boltzmann method, Phys. Fluids **31**, 042105 (2019).

[36] G. Wang, J. Gao, and K. H. Luo, Droplet impacting a superhydrophobic mesh array: Effect of liquid properties, Phys. Rev. Fluids **5**, 123605 (2020).

[37] See Supplemental Material at http://link.aps.org/supplemental/10.1103/PhysRevE.105.045314 for explicit expressions of transformation matrixes and shift matrixes for D3Q19 and D3Q27 models.

[38] M. Geier, A. Greiner, and J. G. Korvink, Cascaded digital lattice Boltzmann automata for high Reynolds number flow, Phys. Rev. E - Stat. Nonlinear, Soft Matter Phys. **73**, 066705 (2006).

[39] L. Fei and K. H. Luo, Consistent forcing scheme in the cascaded lattice Boltzmann method, Phys. Rev. E **96**, 053307 (2017).

[40] X. He, S. Chen, and G. D. Doolen, A novel thermal model for the lattice Boltzmann method in incompressible limit, J. Comput. Phys. **146**, 282 (1998).

[41] F. Bösch, S. S. Chikatamarla, and I. V. Karlin, Entropic multirelaxation lattice Boltzmann models for turbulent flows, Phys. Rev. E - Stat. Nonlinear, Soft Matter Phys. **92**, 043309 (2015).

[42] F. Qin, A. Mazloomi Moqaddam, Q. Kang, D. Derome, and J. Carmeliet, Entropic multiple-relaxation-time multirange pseudopotential lattice Boltzmann model for two-phase flow, Phys. Fluids **30**, 032104 (2018).

[43] R. Zhang and H. Chen, Lattice Boltzmann method for simulations of liquid-vapor thermal flows, Phys. Rev. E **67**, 066711 (2003).

[44] C. E. Colosqui, G. Falcucci, S. Ubertini, and S. Succi, Mesoscopic simulation of non-ideal fluids with self-tuning of the equation of state, Soft Matter **8**, 3798 (2012).

[45] Q. Li and K. H. Luo, Thermodynamic consistency of the pseudopotential lattice Boltzmann model for simulating liquid-vapor flows, Appl. Therm. Eng. **72**, 56 (2014).

[46] A. Hu, L. Li, and R. Uddin, Force method in a pseudo-potential lattice Boltzmann model, J. Comput. Phys. **294**, 78 (2015).

[47] X. Shan, Pressure tensor calculation in a class of nonideal gas lattice Boltzmann models, Phys. Rev. E - Stat. Nonlinear, Soft Matter Phys. **77**, 066702 (2008).

[48] J. Latt and B. Chopard, Lattice Boltzmann method with regularized pre-collision distribution functions, Math. Comput. Simul. **72**, 165 (2006).

[49] F. Bösch, B. Dorschner, and I. Karlin, Entropic multi-relaxation free-energy lattice Boltzmann model for two-phase flows, epl **122**, 14002 (2018).

[50] Q. Li, K. H. Luo, Q. J. Kang, and Q. Chen, Contact angles in the pseudopotential lattice Boltzmann modeling of wetting, Phys. Rev. E - Stat. Nonlinear, Soft Matter Phys. **90**, 053301 (2014).

[51] J. Yang, X. Ma, L. Fei, X. Zhang, K. H. Luo, and S. Shuai, Effects of hysteresis window on contact angle hysteresis behaviour at large Bond number, J. Colloid Interface Sci. **566**, 327 (2020).

[52] L. Wang, H. B. Huang, and X. Y. Lu, Scheme for contact angle and its hysteresis in a multiphase lattice Boltzmann method, Phys. Rev. E - Stat. Nonlinear, Soft Matter Phys. **87**, 013301 (2013).

[53] J. C. Bird, S. Mandre, and H. A. Stone, Short-Time Dynamics of Partial Wetting, Phys. Rev. Lett. **100**, 234501 (2008).

[54] C. Clanet, C. Béguin, D. Richard, and D. Quéré, Maximal deformation of an impacting drop, J. Fluid Mech. **517**, 199 (2004).

[55] D. Richard, C. Clanet, and D. Quéré, Contact time of a bouncing drop, Nature (London) **417**, 811 (2002).

[56] A. Gauthier, S. Symon, C. Clanet, and D. Quéré, Water impacting on superhydrophobic macrotextures, Nat. Commun. **6**, 8001 (2015).

[57] N. Ashgriz, J. Y. Poo, and G. Britain, Coalescence and separation in binary collisions of liquid drops, J. Fluid Mech. **221**, 183 (1990).

[58] M. Andrew, Y. Liu, and J. M. Yeomans, Variation of the contact time of droplets bouncing on cylindrical ridges with ridge size, Langmuir **33**, 7583 (2017).

[59] Y. Liu, L. Moevius, X. Xu, T. Qian, J. M. Yeomans, and Z. Wang, Pancake bouncing on superhydrophobic surfaces, Nat. Phys. **10**, 515 (2014).

[60] J. Song, M. Gao, C. Zhao, Y. Lu, L. Huang, X. Liu, C. J. Carmalt, X. Deng, and I. P. Parkin, Large-area fabrication of droplet pancake bouncing surface and control of bouncing state, ACS Nano **11**, 9259 (2017).

[61] L. Moevius, Y. Liu, Z. Wang, and J. M. Yeomans, Pancake bouncing: Simulations and theory and experimental verification, Langmuir **30**, 13021 (2014).

[62] C. K. Kuan, K. L. Pan, and W. Shyy, Study on high-Weber-number droplet collision by a parallel, adaptive interface-tracking method, J. Fluid Mech. **759**, 104 (2014).

[63] K. L. Pan, P. C. Chou, and Y. J. Tseng, Binary droplet collision at high Weber number, Phys. Rev. E - Stat. Nonlinear, Soft Matter Phys. **80**, 036301 (2009).

[64] M. Liu and D. Bothe, Numerical study of head-on droplet collisions at high Weber numbers, J. Fluid Mech. **789**, 785 (2016).

[65] Y. Wu, Q. Wang, and C. Y. Zhao, Three-dimensional droplet splashing dynamics measurement with a stereoscopic shadowgraph system, Int. J. Heat Fluid Flow **83**, 108576 (2020).

[66] I. V Karlin, A. Ferrante, and H. C. Öttinger, Perfect entropy functions of the lattice Boltzmann method, Europhys. Lett. **47**, 182 (1999).